AGU PUBLICATIONS

JGR

Journal of Geophysical Research: Space Physics

RESEARCH ARTICLE
10.1002/2017JA024294

Key Points:
- When interplanetary magnetic field is southward, cusp/mantle dynamo is activated, which supplies electromagnetic energy to magnetosphere
- Integral curve of Poynting flux coming from cusp/mantle dynamo shows a spiral toward Earth, suggesting pathway of electromagnetic energy
- At onset, near-Earth dynamo is embedded in pathway from cusp/mantle dynamo to ionosphere and responsible for onset field-aligned current

Correspondence to:
Y. Ebihara,
ebihara@rish.kyoto-u.ac.jp

Citation:
Ebihara, Y., & Tanaka, T. (2017). Energy flow exciting field-aligned current at substorm expansion onset. *Journal of Geophysical Research: Space Physics*, *122*, 12,288–12,309. https://doi.org/10.1002/2017JA024294

Received 24 APR 2017
Accepted 28 NOV 2017
Accepted article online 4 DEC 2017
Published online 22 DEC 2017

Energy Flow Exciting Field-Aligned Current at Substorm Expansion Onset

Y. Ebihara[1] **and T. Tanaka**[2]

[1]Research Institute for Sustainable Humanosphere, Kyoto University, Uji, Japan, [2]International Center for Space Weather Science and Education, Kyushu University, Fukuoka, Japan

Abstract At substorm expansion onset, upward field-aligned currents (FACs) increase abruptly, and a large amount of electromagnetic energy starts to consume in the polar ionosphere. A question arises as to where the energy comes from. Based on the results obtained by the global magnetohydrodynamics simulation, we present energy flow and energy conversion associated with the upward FACs that manifest the onset. Our simulations show that the cusp/mantle region transmits electromagnetic energy to almost the entire region of the magnetosphere when the interplanetary magnetic field is southward. Integral curve of the Poynting flux shows a spiral moving toward the ionosphere, probably suggesting the pathway of electromagnetic energy from the cusp/mantle dynamo to the ionosphere. The near-Earth reconnection initiates three-dimensional redistribution of the magnetosphere. Flow shear in the near-Earth region results in the generation of the near-Earth dynamo and the onset FACs. The onset FACs are responsible to transport the electromagnetic energy toward the Earth. In the near-Earth region, the electromagnetic energy coming from the cusp/mantle dynamo is converted to the kinetic energy (known as bursty bulk flow) and the thermal energy (associated with high-pressure region in the inner magnetosphere). Then, they are converted to the electromagnetic energy associated with the onset FACs. A part of electromagnetic energy is stored in the lobe region during the growth phase. The release of the stored energy, together with the continuously supplied energy from the cusp/mantle dynamo, contributes to the energy supply to the ionosphere during the expansion phase.

Plain Language Summary In the polar region, sudden brightening and quick spread of aurora can be seen. This is called substorm expansion. The bright aurora is caused by electrons accelerated in the region of upward field-aligned electric current. Generation of the upward field-aligned current is one of the controversial issues in the substorm research. In order to generate the field-aligned current, dynamo must exist somewhere in the magnetosphere. By using numerical simulation, we identified the pathway and conversion of energy from the solar wind to the ionosphere. When the interplanetary magnetic field turns southward, the cusp/mantle dynamo starts to supply energy persistently into the magnetosphere to activate the large-scale magnetospheric convection. For a while, the near-Earth dynamo, initiated by the near-Earth reconnection, appears to generate the onset field-aligned current. The pathway of the energy is a spiral from the cusp/mantle dynamo to the ionosphere. Just before the onset, a part of the spiral starts to show a significant kink on the nightside, which is associated with the onset field-aligned current and the near-Earth dynamo.

1. Introduction

Sudden brightening of an aurora followed by the formation of an auroral bulge and a traveling surge is known as the onset of a substorm expansion phase (Akasofu, 1964). The bright aurora that characterizes the substorm expansion phase is primarily caused by precipitation of electrons accelerated toward the Earth. Observations have shown that the accelerated electrons in bright aurorae are associated with upward field-aligned currents (FACs) (e.g., Armstrong, Akasofu, & Rostoker, 1975; Arnoldy, 1974; Murphy et al., 2013; Sakanoi, Fukunishi, & Mukai, 1995). The upward FACs connect with the ionospheric current, which appears to be an auroral electrojet (e.g., Atkinson, 1967; Boström, 1964; Connors et al.,2014; Gjerloev & Hoffman, 2014; Kamide & Akasofu, 1976; Kamide, Richmond, & Matsushita, 1981; Rostoker et al., 1975, references therein). The sudden intensification of the westward electrojet is regarded as additional manifestation of the onset of the substorm expansion phase (e.g., Kamide & Akasofu, 1975). A huge amount of electromagnetic energy consumes in the ionosphere. Using ground-based magnetometer data and the ionospheric conductivity inferred from the Dynamics Explorer 1 satellite, Kamide et al. (1986) estimated the Joule heating

production rate to be ~6–9 × 10^{11} W. The ultimate source of the energy that consumes in the polar ionosphere during the substorm expansion is the solar wind, but the energy flow from the solar wind to the ionosphere is still unclear. One of the keys in understanding the energy flow is the FACs, in particular, suddenly enhanced FACs because the FACs are known to guide the electromagnetic energy to go into the ionosphere (e.g., Strangeway et al., 2000).

1.1. Origin of Onset FAC

The current wedge model has been applied to understand the sudden intensification of FACs associated with the expansion phase onset (e.g., Kepko et al., 2015; McPherron & Chu, 2016; McPherron, Russell, & Aubry, 1973). The current wedge consists of a pair of FACs in which a downward current flows into the ionosphere on the dawnside and an upward current flows out of the ionosphere on the duskside. Thus, the polarity of the current wedge is the same as that of the Region 1 FAC (Iijima & Potemra, 1976). The downward and upward FACs connect with the cross-tail current that flows westward in the equatorial plane. The current wedge is thought to appear when the cross-tail current is deviated and "short circuited" to the ionosphere. The current wedge model was recently revised (Kepko et al., 2015). A major revision from the original picture drawn by McPherron et al. (1973) is the addition of Region 2-sence FACs earthward of the Region 1-sense FACs. The formation of the current wedge is most likely related to magnetospheric processes but is still one of the central issues in the substorm study.

A near-Earth neutral line (NENL) is known to be closely associated with substorms (e.g., Hones Jr. et al., 1973; Nishida & Nagayama, 1973). Based on the concept of bulk "motion" of magnetic field lines (e.g., Brice, 1967; Dungey, 1961), it has been thought that a substorm expansion onset is triggered when the merging rate in the tail exceeds that on the dayside magnetosphere and that the onset is regarded as release of magnetic energy stored in the tail (e.g., Russell & McPherron, 1973; Schindler, 1974). In the vicinity of the NENL, strong flow vorticities and FACs (Baker et al., 1993) and a Hall current system (e.g., Treumann et al., 2006) are suggested to appear. Recent particle-in-cell simulations have shown that kinetic Alfvén waves are transmitted from the reconnection region, which probably reach the bright aurora (Shay et al., 2011).

If one assumes that the FACs are generated in the vicinity of the NENL, that is, the current wedge overlapping with the NENL, one will encounter a problem in explaining the position of the expansion onset (Lui, 1991). Auroral observations have shown that the expansion onset starts near the equatorward boundary of the auroral oval, that is, well equatorward of the open-closed boundary (e.g., Elphinstone et al., 1991; Kadokura et al., 2002; Lui & Burrows, 1978; Samson et al., 1992; Samson et al., 1992). A current disruption model attempts to explain the position of the expansion onset without introducing the NENL (Lui, 1996). The current disruption is supported by the observation of large-amplitude oscillations of the magnetic field in the near-Earth plasma sheet at a radial distance of ~8 *Re* at the onset (e.g., Takahashi et al., 1987). Data from Time History of Events and Macroscale Interactions during Substorms (THEMIS) satellites show that the current density was rapidly decreased by ~40% in the neutral sheet with a timescale of seconds at $X_{GSM} = -8.1$ *Re*, and the frozen-in condition was broken down (Lui, 2011). Major characteristics of the current disruption can be summarized as follows: large changes in the electric field and magnetic field with a broad frequency range, reduction in the cross-tail current, no propagation of the current disruption from the tail region, and breakdown of the magnetohydrodynamics (MHD) assumption (Lui, 1996). The current disruption is suggested to take place in association with unloading instability (Kan, 1993), ballooning instability (Pu, Korth, & Kremser, 1992; Roux et al., 1991; Xing et al., 2013; Xing & Wolf, 2007; Yue et al., 2015), or cross-field current instability (Lui et al., 1991). When the current disruption occurs, Region 1-sense FACs are generated in the current disruption region by the requirement of the current continuity (Lui, 1996). The magnetic energy stored in the lobe supplies electromagnetic energy to the current disruption region as a series of fast-mode waves (Lui, 1996).

Some NENL-based models may resolve the problem of the onset position. If an earthward flow channel, or burst coming from the NENL (e.g., Hones, 1984), consists of low-entropy plasma (bubble), the cross-tail current must be connected with Region 1-sense FACs to maintain the current continuity (e.g., Birn et al., 2004, 2011; Chen & Wolf, 1993; Wolf et al., 2009; Yang et al., 2012). As the earthward flow channel approaches the inner magnetosphere, the tailward force decelerates the plasma moving earthward. The consequent inertial current may connect with the Region 1-sense FACs (Haerendel, 1992; Shiokawa, Baumjohann, &

Haerendel, 1997). This process may be equivalent to energy conversion from bulk flow energy to electromagnetic energy. According to simulations (Birn & Hesse, 1991; Birn et al., 2004, 2011), the earthward flow channel splits into two directions, and each of them deflects toward dawnside and duskside. The directional change results in the flow vorticity (shear), which may favor in leading the generation of the Region 1-sense FACs. Such flow vorticity (shear) in the equatorial plane has been observed and thought to lead to the onset FACs (Keiling et al., 2009; Yao et al., 2012). It is a general presumption in these models that the onset FACs come from the equatorial plane along a field line. On the contrary, it is shown that the current line deviates from the magnetic field line at off-equator (Tanaka, 2015) and that the vortex being responsible for the onset FAC appears at off-equatorial low-altitude region (Ebihara & Tanaka, 2015a).

1.2. Dynamo for Onset FAC

In the ionosphere, the Joule dissipation is known to increase at onset (e.g., Ahn et al., 1983; Kamide, Sun, & Akasofu, 1996; Østgaard et al., 2002; Palmroth et al., 2005; Richmond et al., 1990; Tanskanen et al., 2005; Zhou et al., 2011). A question arises as to where the energy comes from. It has been shown that the solar wind parameter, ε, known as the energy coupling function probably reflecting the excitation rate of the dynamo, correlates with the *AE* index (Akasofu, 1979a) and power consumption in the magnetosphere (Kan, Lee, & Akasofu, 1980). The ε parameter is defined by the equation $\varepsilon = VB^2\sin^4(\theta/2){l_0}^2$, where V, B, θ, and l_0 are the solar wind speed, the interplanetary magnetic field, the clock angle of the interplanetary magnetic field ($\equiv \tan^{-1}(B_y/B_z)$), and a constant length being 7 *Re*, respectively. A substorm onset is suggested to take place when ε exceeds ~10^{18} erg/s (~10^{11} W) (Akasofu, 1980). Kan et al. (1980) emphasized that a substorm is a direct consequence of the enhancement of power out from the dynamo located in the magnetotail. With regard to transmission of energy from the solar wind to the magnetosphere, Akasofu et al. (1981) suggested the following processes. When the solar wind passes through the magnetic field on the magnetopause, the electric field associated with the electromotive force provides electric potential at the magnetopause. The electric power is transmitted to the convective motion of plasma in the magnetosphere. The convective motion of plasma in the tail acts as the MHD dynamo that generates FACs connecting with the ionosphere. Geotail satellite observations show that ion bulk velocity, particle pressure, thermal energy flux, and field-aligned current increase with the ε parameter (Kaufmann, 2012). However, as far as we know, the energy flow and the dynamo regions that are related to the expansion onset have not been confirmed by observations.

Akasofu (2003, 2015) further considered the dynamo in the tail region. He started with a pair of field-aligned current sheets known as Boström's Type 2 current (Boström, 1964). Upward current sheet is located equatorward of downward one. This type of the current system was not considered by Kepko et al. (2015). In order to maintain the current continuity, the radially outward current must flow to connect the two current sheets in the magnetosphere. Akasofu (2003, 2015) has assumed that the electric field pointing inward (earthward) exists in the magnetosphere. The direction of the electric field **E** is opposite to that of the current **J**, indicating a dynamo ($\mathbf{J}\cdot\mathbf{E} < 0$). An immediate question is concerned with the generation of the electric field pointing inward (earthward). Some external forces must work to set up the dynamo. Lui and Kamide (2003) suggested that during the dipolarization, magnetized electrons move earthward together with the motion of the magnetic field, whereas unmagnetized ions remain. This causes charge separation. Positive charge is concentrated in the outer region and negative charge in the inner region. The charge separation caused by nonmagnetized motion of ions gives rise to the earthward directed electric field, generating a dynamo ($\mathbf{J}\cdot\mathbf{E} < 0$).

Miyashita et al. (2001) performed a statistical study on the mass and energy transport in the near-Earth tail region on the basis of the data from Geotail. The expansion onset was defined by Pi2 pulsations. A large amount of energy starts to be transported from the lobe to the plasma sheet in the form of the Poynting flux about 0–2 min before the expansion onset. The kinetic energy flux is minor in comparison with the Poynting flux. Haerendel (2009) proposed a concept of squeezing of the magnetosphere. When the stretched magnetic field becomes dipole-like, a thin layer of the high-beta region is expected to cover the outer boundary surface of the dipolar magnetosphere near 7–8 *Re*. This thin layer is squeezed from the outside by the high magnetic field in the lobe. The magnetic energy is released in the tail and is fed into the thermal energy. The thermal energy is then fed into the load in the ionosphere. The loss of the thermal energy by Poynting flux toward the ionosphere results in the recovery of the magnetic field configuration.

1.3. Dynamo Predicted by Global MHD Simulation

Three-dimensional distribution of the current system and related dynamo was first provided by Tanaka (1995) who solved the MHD equation with magnetosphere-ionosphere coupling in a self-consistent manner. This approach made the magnetospheric dynamo clear. From this method, Tanaka (1995) and Siscoe et al. (2000) pointed out that the cusp/mantle region is the significant dynamo region in the magnetosphere to drive the current system associated with the Region 1 FACs and to drive the convection. This is different from the view in which the Region 1 FACs are mapped along a field line to the low-latitude boundary layer where a viscous-like interaction between the solar wind and the magnetosphere occurs (Axford & Hines, 1961). Wing et al. (2010) investigated precipitating particles and FACs and found that the Region 1 FACs are mapped to the low-latitude boundary layer at noon and the plasma sheet boundary in the morning and afternoon regions. The difference may come from the inclusion of the perpendicular current. The Region 1 current is almost field aligned at low altitude, whereas it will be diverted from the original field line by the perpendicular current. Based on the consideration that the convection, plasma regimes, the dynamo, and the FAC should be organized in a self-consistent manner, Tanaka (2007) and Tanaka et al. (2016) suggest the following mechanism for the solar wind-magnetosphere interaction. Behind the bow shock, deceleration and pressure gradient along the streamline inside the magnetosheath contribute to the generation of Poynting flux. This Poynting flux is transported inside the magnetosphere to result in an increase in the plasma pressure in the cusp. Thermal energy stored inside the cusp is then converted to the electromagnetic energy for the region 1 FAC through the slow-mode expansion. This dynamo works steadily even during the substorm cycle.

From the results of the substorm simulation, at least three dynamo regions are identified, including the cusp/mantle dynamo. First, the cusp/mantle dynamo supplies electromagnetic energy when interplanetary magnetic field (IMF) is southward or during the substorm growth phase (Tanaka, 2015; Tanaka et al., 2010). Second, the near-Earth dynamo appears at the onset of substorm expansion (Birn & Hesse, 2005; Ebihara & Tanaka, 2015a; Tanaka, 2015). Birn and Hesse (2005) showed that the energy conversion takes place in multiple steps. The magnetic energy in the lobe is converted to the bulk kinetic energy through the reconnection. The bulk kinetic energy is then converted to the thermal energy and successively converted to electromagnetic energy in the near-Earth dynamo. Third, the dynamo action starts to appear near the interface between the magnetosphere and the ionosphere when the ionospheric Hall current has a large gradient (Ebihara & Tanaka, 2015b, 2018). During the expansion phase, the ionospheric Hall conductivity is locally enhanced, resulting in overflow of the ionospheric Hall current and charge accumulation near the conductivity gradient (bright aurora) (e.g., Fujii et al., 2011; Kan, Williams, & Akasofu, 1984; Kan & Kamide, 1985; Kan & Sun, 1996). Ebihara and Tanaka (2015b) showed that a westward traveling surge appears in the global MHD simulation and that the dynamo associated with the overflow of the ionospheric Hall current is essential for the formation of the westward traveling surge.

The global MHD simulation has made the current system and the dynamo regions clear. On the analogy of an electrocircuit, the dynamo feeds electromagnetic energy, which is consumed in the load. However, the electromagnetic energy is not directly fed from the cusp/mantle dynamo into the ionosphere because energy conversions are suggested to occur in the region between them, according to the global MHD simulation (Birn & Hesse, 2005; Ebihara & Tanaka, 2015a; Tanaka, 2015). The pathway of the energy from the dynamo to the ionosphere and associated energy conversion are still unclear and controversial. The purpose of this study is to investigate the energy flow and the energy conversion to understand the expansion onset in terms of energetics.

2. Methodology

2.1. Global MHD Simulation

We solved the global MHD simulation developed by Tanaka (2015) and used the same simulation results obtained by Ebihara and Tanaka (2015a). The inner boundary of the magnetospheric domain is located on a spherical surface at 2.6 *Re*, and the outer boundary is located at 200 *Re* at midnight and 600 *Re* at noon. In order to concentrate the number of grid points on the nightside, the outer boundary is deformed. The total variation diminishing scheme was applied for the MHD equations (Tanaka, 1995). The present simulation is designed to realize high resolution for the calculation of the FAC. In order to obtain such performance, the

unstructured grid with no apparent singularity is most essential. First, we divided the sphere at the inner boundary into 12 pentagons. A pentagon was further divided into five triangles. The number of triangles is 60. This is called Level 1. A triangle was further divided into four, which is called Level 2. We used Level 6 in which a sphere was divided into 61,440 triangles because of the following reasons. With regard to the onset mechanism, the simulation result is essentially the same as that obtained with Level 7 as shown in Ebihara and Tanaka (2015b). In order to display three-dimensional perspective view of the magnetosphere, we used a computer software, named VisIT. Data from the Level 7 simulation are too large, so that VisIT cannot handle the data for the three-dimensional rendering. To develop a three-dimensional grid, we stacked the triangular prisms 320 times. We mapped field-aligned current and plasma pressure from the inner boundary of the magnetospheric domain to the ionosphere along a dipole magnetic field line. The field-aligned current and the plasma pressure were used to estimate the ionospheric conductivity tensor. The detailed information about the calculation of the ionospheric conductivity is described by Ebihara, Tanaka, and Kikuchi (2014). For the mapped field-aligned current $J_\parallel$ and the ionospheric conductivity tensor Σ, we solved the following elliptic partial differential equation to obtain the ionospheric electric potential Φ_i with satisfaction of the current continuity as

$$\nabla\cdot\Sigma(\nabla\Phi_i) = J_\parallel. \tag{1}$$

The ionospheric potential is mapped to the inner boundary of the magnetospheric domain and is used to determine the boundary condition at the inner boundary. The solar wind parameters used are as follows. At t = 0, the Z component of the interplanetary magnetic field (IMF) was changed from +5 nT to −5 nT, and the solar wind speed was increased from 372 to 500 km s^{-1} at X = 39 *Re*. The solar wind density and Y component of the IMF were kept constant at 5 cm^{-3} and 2.5 nT, respectively. All of the simulation settings, grid systems, and ionospheric conductivities were the same as those used by Ebihara et al. (2014) and Ebihara and Tanaka (2015a). Following Ebihara and Tanaka (2015a), the onset of the substorm expansion was identified on the basis of the sudden intensification of the upward FAC close to midnight. The onset occurred at 66.7 magnetic latitude (MLAT) and 2318 magnetic local time (MLT) at t ~ 57.3 min. More detailed information about the simulation setting can be found in Ebihara and Tanaka (2015a).

2.2. Related Equations

The global MHD simulation solves the evolution of the eight variables, including the mass density ρ, the plasma pressure P, the velocity **V**, and the magnetic field **B**. The plasma pressure is assumed to be isotropic and a scalar in the simulation. In the ideal MHD, the electric field **E** is given by

$$\mathbf{E} = -\mathbf{V}\times\mathbf{B}, \tag{2}$$

and the current density **J** is given by

$$\mathbf{J} = \frac{1}{\mu_0}\nabla\times\mathbf{B}, \tag{3}$$

where μ_0 is the magnetic constant.

From Faraday's law and Ampère's law, the equation that describes the generation of the FAC$J_\parallel$ is given by

$$\frac{\partial J_\parallel}{\partial t} = -\frac{1}{\mu_0}[\nabla\times\nabla\times\mathbf{E}]_\parallel. \tag{4}$$

Equation (4) yields (Song & Lysak, 2001a, 2001b)

$$\frac{\partial J_\parallel}{\partial t} = \frac{1}{\mu_0}\left[-\nabla(\nabla\cdot\mathbf{E}) + \nabla^2\mathbf{E}\right]_\parallel = \frac{1}{\mu_0}\left[\nabla_\parallel(\nabla_\perp\cdot(\mathbf{V}\times\mathbf{B})) + {\nabla_\perp}^2 E_\parallel\right] = \frac{1}{\mu_0}\left[\nabla_\parallel(\mathbf{B}\cdot(\nabla_\perp\times\mathbf{V}) + \mathbf{V}\cdot(\nabla_\perp\times\mathbf{B})) + {\nabla_\perp}^2 E_\parallel\right]$$
$$= \frac{1}{\mu_0}\left[\nabla_\parallel(\mathbf{B}\cdot\boldsymbol{\Omega}_\parallel + \mu_0\mathbf{V}\cdot\mathbf{J}_\perp) + {\nabla_\perp}^2 E_\parallel\right]. \tag{5}$$

Here we defined the vorticity as $\boldsymbol{\Omega} \equiv \nabla\times\mathbf{V}$. In the ideal MHD, the last term on the right-hand side of equation (5) vanishes. For simplicity, we assumed that the second term is negligibly small (Song & Lysak,

2001a, 2001b). We confirmed that the second term is about 2 orders magnitude smaller than the first term along the magnetic field line extending from the onset position. Then, equation (5) yields

$$\begin{aligned}\frac{\partial J_\parallel}{\partial t} &\cong \frac{1}{\mu_0}\nabla_\parallel(B\Omega_\parallel)\\ &= \frac{1}{\mu_0}\frac{\mathbf{B}}{B}\cdot\nabla(B\Omega_\parallel)\\ &= \frac{1}{\mu_0}\frac{\mathbf{B}}{B}\cdot[B\nabla\Omega_\parallel + \Omega_\parallel\nabla B]\\ &\cong \frac{1}{\mu_0}\mathbf{B}\cdot\nabla\Omega_\parallel.\end{aligned} \tag{6}$$

We assumed that the term $\Omega_\parallel\nabla B$ is negligible because the term $\Omega_\parallel\nabla B$ is about 20–30% smaller than the term $B\nabla\Omega_\parallel$, for example, in the region where the onset FACs are generated in the near-Earth region.

The momentum equation is given by

$$\rho\frac{\mathrm{d}\mathbf{V}}{\mathrm{d}t} = \mathbf{J}\times\mathbf{B} - \nabla P. \tag{7}$$

The first term of the right-hand side is called Lorentz force. The second term is called pressure gradient force. The plasma pressure is assumed to be isotropic and a scalar in the simulation. Regardless of this assumption, the simulation is capable of reproducing many observable features that manifest the substorm expansion (Ebihara & Tanaka, 2015a, 2015b; Tanaka, 2015; Tanaka et al., 2010, 2016). Of course, the validity of the assumption, isotropic plasma pressure, should be evaluated in the future.

By taking the curl of equation (7), we obtain the equation that describes the generation of the vorticity.

$$\begin{aligned}\nabla\times\left(\rho\frac{\mathrm{d}\mathbf{V}}{\mathrm{d}t}\right) &= \nabla\times(\mathbf{J}\times\mathbf{B})\\ \rho\nabla\times\frac{\mathrm{d}\mathbf{V}}{\mathrm{d}t} &= \nabla\times(\mathbf{J}\times\mathbf{B}) - \nabla\rho\times\frac{\mathrm{d}\mathbf{V}}{\mathrm{d}t}\\ \frac{\mathrm{d}\boldsymbol{\Omega}}{\mathrm{d}t} &= \frac{1}{\rho}\nabla\times(\mathbf{J}\times\mathbf{B}) - \frac{1}{\rho}\nabla\rho\times\frac{\mathrm{d}\mathbf{V}}{\mathrm{d}t}.\end{aligned} \tag{8}$$

In accordance with Faraday's law, the rate of change in the magnetic field is given by

$$\begin{aligned}\frac{\partial\mathbf{B}}{\partial t} &= \nabla\times(\mathbf{V}\times\mathbf{B})\\ &= -(\mathbf{V}\cdot\nabla)\mathbf{B} + (\mathbf{B}\cdot\nabla)\mathbf{V} - \mathbf{B}(\nabla\cdot\mathbf{V}).\end{aligned} \tag{9}$$

The rate of change in the plasma pressure ($\partial P/\partial t$) is given by

$$\frac{\partial P}{\partial t} = -(\mathbf{V}\cdot\nabla)P - \gamma P\nabla\cdot\mathbf{V}, \tag{10}$$

where Γ is the ratio of specific heat (= 5/3). The first and second terms on the right-hand side are associated with advection and compression, respectively.

Regarding the electromagnetic energy, we used Poynting's theorem as

$$\begin{aligned}\nabla\cdot\mathbf{S} &= -\frac{\partial}{\partial t}\left(\frac{B^2}{2\mu_0}\right) - \mathbf{J}\cdot\mathbf{E}\\ &= -\frac{\partial}{\partial t}\left(\frac{B^2}{2\mu_0}\right) - \mathbf{V}_\perp\cdot(\mathbf{J}\times\mathbf{B}),\end{aligned} \tag{11}$$

where

$$\mathbf{S}\equiv\frac{\mathbf{E}\times\mathbf{B}}{\mu_0}. \tag{12}$$

S is called a Poynting flux. By taking a scalar product of the velocity **V** with equation (7) and the continuity equation for mass, the transport equation of the bulk flow is given by

$$\frac{\partial}{\partial t}\left(\frac{\rho}{2}V^2\right) = -\nabla\cdot\left(\frac{\rho}{2}V^2\mathbf{V}\right) + \mathbf{V}\cdot(\mathbf{J}\times\mathbf{B} - \nabla P), \tag{13}$$

where $V = |\mathbf{V}|$. The second term on the right-hand side governs the conservation of the kinetic energy and mediates the energy transfer from another. From equation (7) and the continuity equation for mass, the transport of thermal energy is given by

$$\frac{\partial u}{\partial t} = -\nabla\cdot(\gamma u\mathbf{V}) + \mathbf{V}\cdot\nabla P. \tag{14}$$

where u is the thermal energy ($\equiv 3P/2$). The second term on the right-hand side governs the conversation of the thermal energy. Following Birn and Hesse (2005), we defined enthalpy flux **H** and bulk kinetic flux **K** as

$$\mathbf{H} = \gamma u\mathbf{V} \tag{15}$$

and

$$\mathbf{K} = \frac{1}{2}\rho V^2\mathbf{V}, \tag{16}$$

respectively.

3. Results

3.1. Evolution of Field-Aligned Current, Auroral Electrojet, and Joule Dissipation in the Ionosphere

Figure 1 shows the calculated *AU* and *AL* indices and the FACs at the ionospheric altitude. We calculated the magnetic disturbance on the ground at 48 different magnetic local times (MLTs) at 67° magnetic latitude (MLAT). The magnetic disturbance was calculated on the basis of the ionospheric Hall current that is given by $\mathbf{J}_H = \Sigma_H\mathbf{E}_i$, where Σ_H is the Hall conductivity. $\mathbf{E}_i$ is the ionospheric electric field given by the equation $\mathbf{E}_i = -\nabla\Phi_i$, where Φ_i is the ionospheric potential that is obtained by solving the elliptic partial differential equation of equation (1). After superposing the 48 temporal variations of the magnetic disturbance, we took a lower bound (envelope) as the *AL* index and an upper bound (envelope) as the *AU* index. The methodology to derive the *AU* and *AL* indices is essentially the same as that proposed by Davis and Sugiura (1966). The calculated *AL* index shows an abrupt decrease at $t \sim 57$ min. (We define $t = 0$ to the moment when the southward IMF arrives at $X = 39$ *Re*.) In the lower half part of Figure 1, the FACs are shown, which are obtained by mapping those at the inner boundary of the magnetospheric domain to the ionosphere along the dipole magnetic field. Before the onset, strong FACs are found on the dayside, which are related to the main part of the Region 1 FACs (Tanaka et al., 2010). The upward FAC is abruptly enhanced in the premidnight at $t \sim 57.3$ min. We call this onset of the expansion phase. The magnitude of the enhanced FAC is largest at 66.7 MLAT and 2318 MLT and is denoted by a cross. The electric potential is indicated by contour lines. The onset takes place in the middle of the Harang discontinuity, which is consistent with observations (e.g., Lyatsky et al., 2001; Nielsen & Greenwald, 1979; Untiedt & Baumjohann, 1993; Weygand et al., 2008; Zou et al., 2009). The FACs associated with the onset increase with time.

Figure 2 shows the radial component of the Poynting flux on the spherical surface at the geocentric distance of 3.5 *Re* and the Joule heating rate in the ionosphere. In Figure 2 (top row), negative values mean the Poynting flux pointing earthward. The earthward Poynting flux appears to increase near midnight at onset. It is speculated that a large part of the earthward Poynting flux would penetrate into the ionosphere, and the electromagnetic energy would consume in the ionosphere. Indeed, the Joule heating rate increases near midnight in the ionosphere at onset, which is consistent with the observations (e.g., Kamide et al., 1996).

3.2. Global Pathway of Electromagnetic Energy

Figure 3 shows a perspective view of the magnetosphere. The coordinates are the same as the Solar Magnetosphere (SM) coordinate system with a dipole tilt angle of 0. The SM coordinate system is centered on the Earth, which has the *X* axis pointing toward the Sun and the *Z* axis being antiparallel to Earth's dipole moment. The *Y* axis is defined as the cross product of the *Z* and *X* axes. The whitish, thick line indicates the integral curve of the Poynting flux **S**. The integral curve of **S** is given by $\int \mathbf{S}\cdot d\mathbf{s}/S$. Hereinafter, we call this

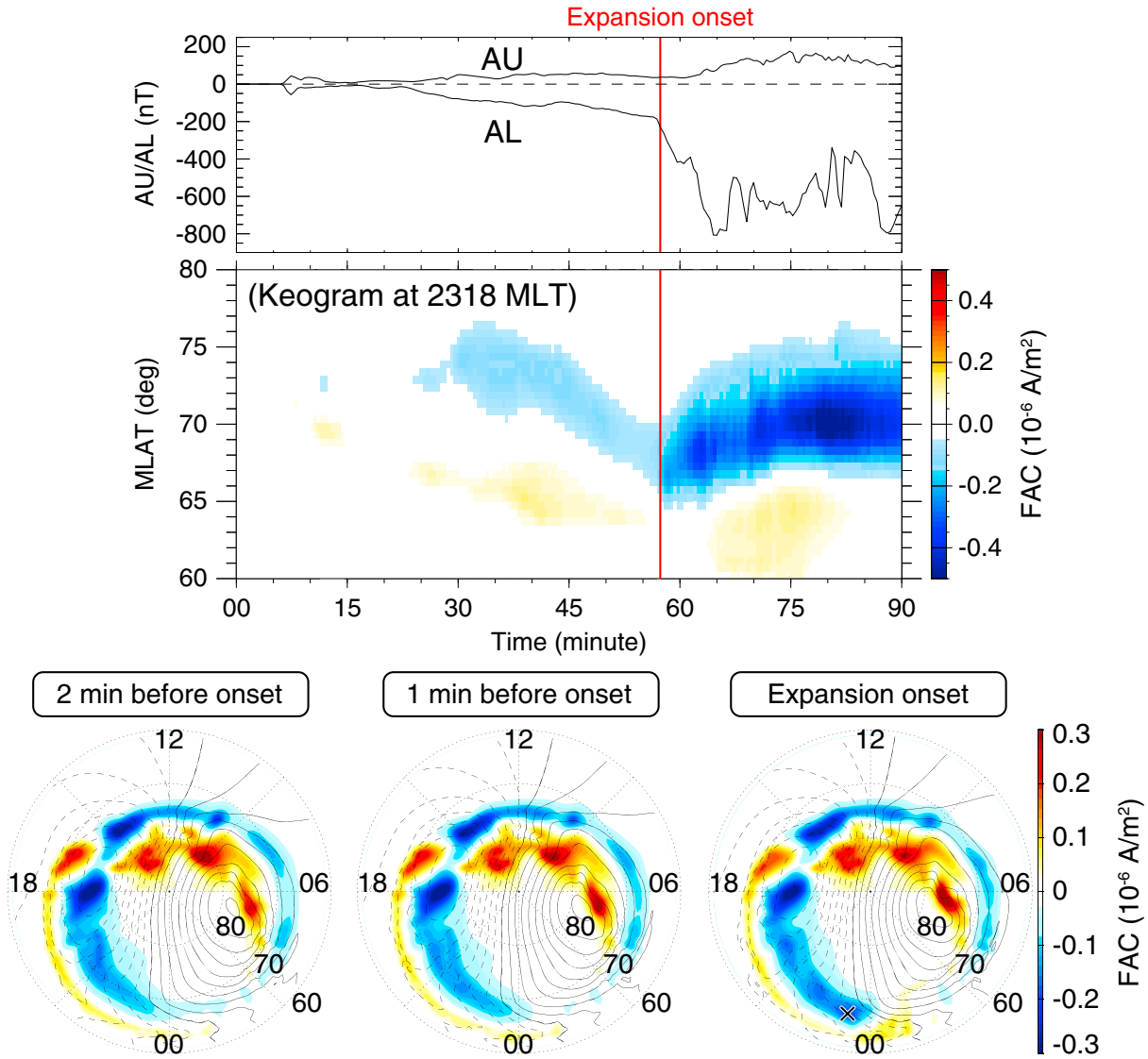

Figure 1. (top) Calculated *AU* and *AL* indices, (middle), a keogram of field-aligned currents (FACs) at 2318 MLT, and (bottom) the FACs at the ionosphere altitude at onset t = 57.3 min, 1 min before onset, and 2 min before onset. In Figure 1 (middle and bottom), blue indicates the upward current, and red indicates the downward current. The contour line in Figure 1 (bottom) denotes the ionospheric electric potential with an interval of 5 kV. The onset position, where the upward FAC suddenly increases, is indicated by the cross. The red line represents the expansion onset time.

an *S*-curve. The *S*-curve presented here is a snapshot, so that *S*-curve is probably different from the actual propagation path of the Poynting flux. No temporal variation is considered in the calculation of the *S*-curve. In spite of the limitation, we think that the *S*-curve is still useful to visualize the instantaneous direction of **S** and to estimate the approximate path of the electromagnetic energy. The light blue line indicates the magnetic field lines. At the onset (Figure 3, right), a near-Earth neutral line (NENL) has formed, and the earthward and tailward flows appear in the equatorial plane. The NENL formed at $X \sim -11.5$ *Re* at $t \sim 48$ min. The location of the NENL is relatively close to the Earth in comparison with most of the observations (e.g., Angelopoulos et al., 2008; Nagai et al., 1998). We believe that the location of the NENL is not so unrealistic. The reason is that near-Earth reconnection taking place at 10–12 *Re* was observed (Sergeev et al., 2008). In the global MHD simulation used by Ebihara and Tanaka (2015b), the NENL took place at $X \sim -42$ *Re* with the solar wind speed of 372 km/s, the solar wind density of 5 cm^{-3}, and IMF B_z of -3 nT. One of the reasons for the different location of NENL may come from different solar wind conditions. We confirmed that the processes are essentially the same with that in the simulation result presented by Ebihara and Tanaka (2015b).

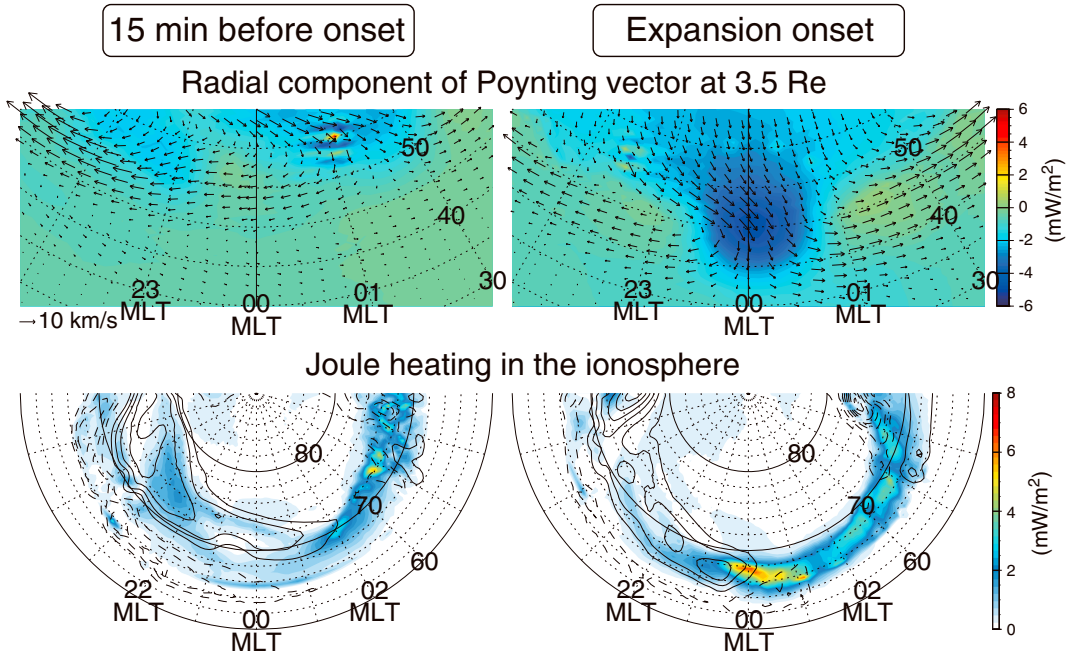

Figure 2. (top row) Radial component of the Poynting flux (positive outward) on the sphere at geocentric distance of 3.5 *Re* and (bottom row) Joule heating in the ionosphere at 15 min before the onset (left column) and onset (right column). In Figure 2 (top row), the arrows indicate the perpendicular flow velocity mapped to the sphere. In Figure 2 (bottom row), the solid and dashed contour lines indicate the upward and downward field-aligned currents, respectively, with an interval of 0.05 μA/m^2. The Sun is to the top.

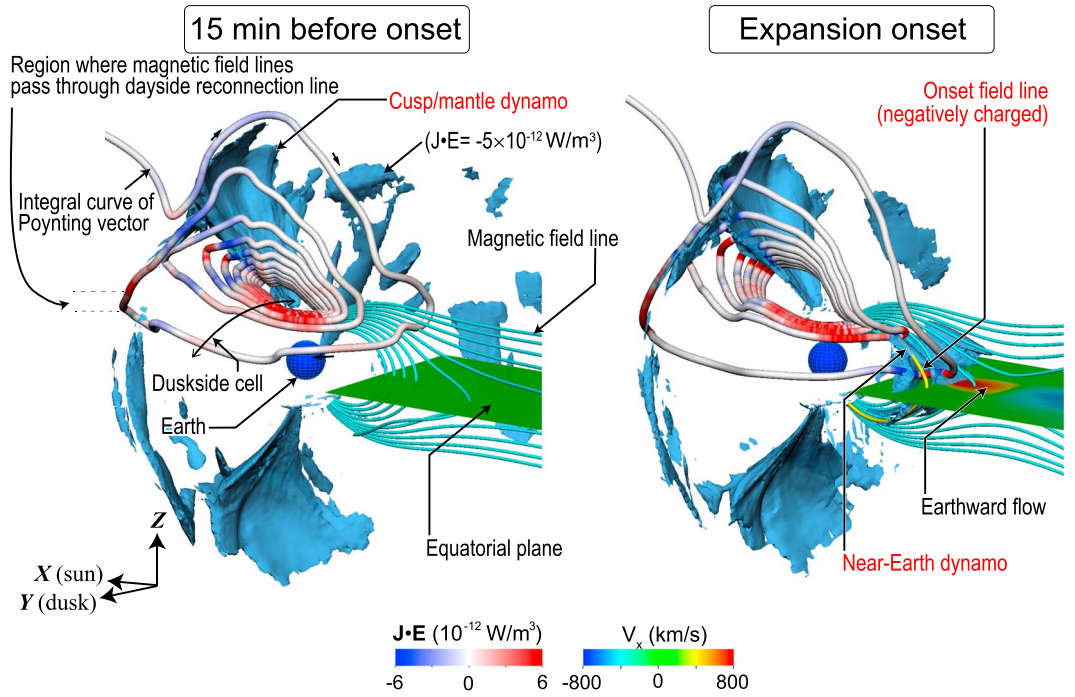

Figure 3. Perspective views of the magnetosphere (left) at 15 min before the expansion onset and (right) at the onset. The whitish, thick line indicates the integral curve of the Poynting flux **S**. The color on the line represents the value of $\mathbf{J} \cdot \mathbf{E}$. The bluish shade represents the region where $\mathbf{J} \cdot \mathbf{E} = -5 \times 10^{12}$ W/m^3 (dynamo region). The thin, yellow line indicates the one extending from the onset position. The thin, blue lines indicate the magnetic field lines extending from the ionosphere at midnight. The *X* component of the plasma velocity is drawn in the equatorial plane. Only the integral curve related to the duskside convection cell is drawn. A similar integral curve, with opposite polarity, exists on the dawnside.

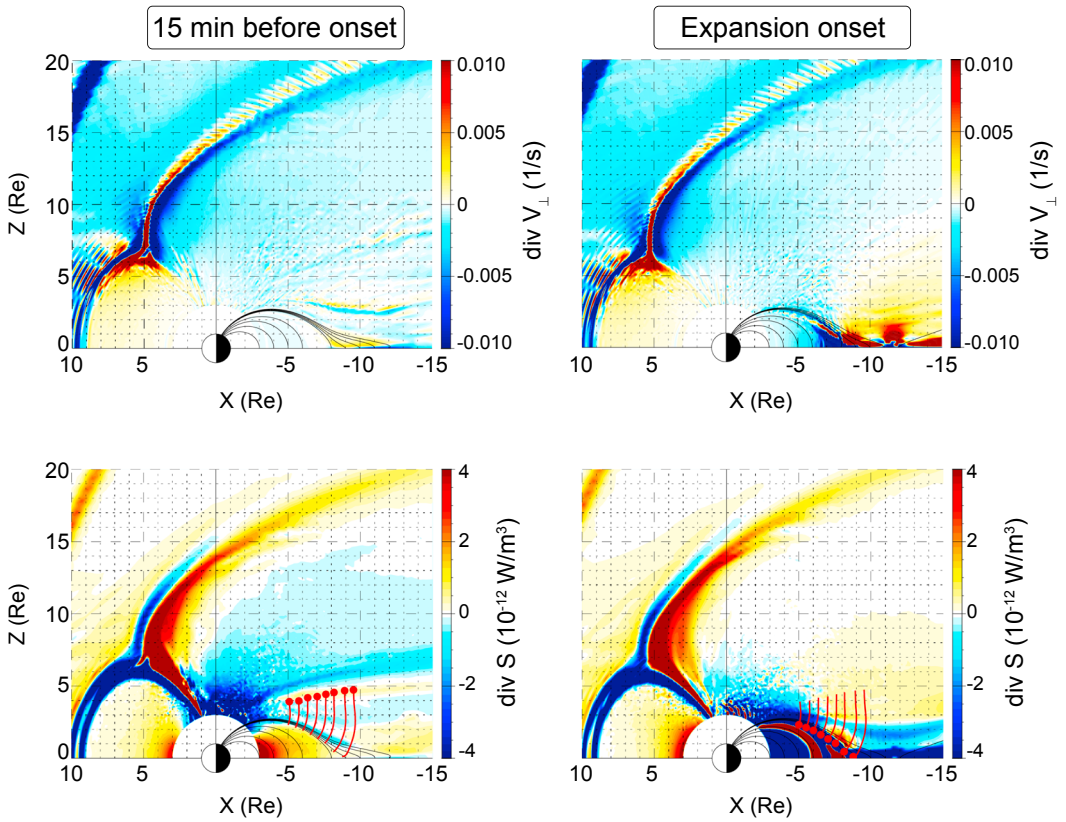

Figure 4. (top row) $\nabla \cdot \mathbf{V}_\perp$ and (bottom row) $\nabla \cdot \mathbf{S}$ in the meridional plane at midnight at 15 min before the expansion onset (left column) and at the onset (right column). The Sun is to the left.

At the onset, the *S*-curve appears to come from the solar wind and passes through the cusp/mantle dynamo region ($\mathbf{J} \cdot \mathbf{E} < 0$) (Siscoe et al., 2000; Tanaka, 1995, 2000). After passing through the cusp/mantle dynamo region where the kinetic energy is converted to the electromagnetic energy, the *S*-curve further travels tailward and toward the equatorial plane. It turns to the west on the nightside. Then, the *S*-curve travels sunward and traverses the region where magnetic field lines pass through the dayside reconnection line. The *S*-curve tends to complete the circular motion but tends to be displaced toward the Earth for every circulation. The *S*-curve shows a sharp kink near the magnetic field line extending from the onset position ("onset field line," the yellow line) and near the near-Earth dynamo. We note that overall, the *S*-curve tends to show a spiral moving toward the Earth. The primary reason for the spiral is the presence of FACs that twist the magnetic field line. The twisted magnetic field line results in the downward (earthward) component of the Poynting flux. The contribution from the Region 2 FACs can also be seen, in general, as a bend in the counterclockwise direction when one views the Earth from space. At 15 min before the onset (Figure 3, left), a sharp kink of the *S*-curve on the nightside is absent. The near-Earth dynamo is also absent.

Figure 3 suggests the following.

1. Large amount of the electromagnetic energy is transmitted from the cusp/mantle dynamo and is transported toward the ionosphere along the *S*-curve. In the sense that the magnetospheric convection is represented by motion of plasma under the $E \times B$ drift, the *S*-curve is an alternative view of the magnetospheric convection because the direction of the $E \times B$ drift is tangential to the *S*-curve.
2. A sharp kink appears near the onset field line, which is closely associated with the negative accumulation of charge or flow vorticity (shear). The kink is a part of the large-scale *S*-curve, which corresponds to the convection in the sense that the convection is represented by the $E \times B$ drift motion.

Figure 3 also shows that the near-Earth dynamo seems to be embedded in the pathway of the energy from the cups/mantle dynamo to the ionosphere. In the sense that the *S*-curve is an alternative view of the

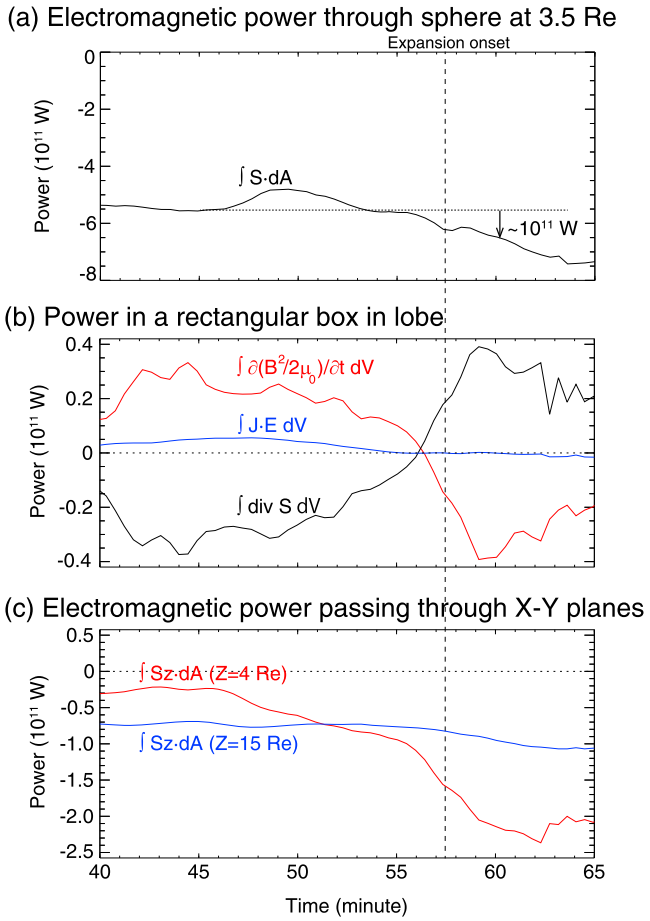

Figure 5. (a) Electromagnetic power passing through the sphere at 3.5 *Re* integrated over the nightside (positive outward), (b) power in a rectangular region in the lobe, and (c) *Z* component of the electromagnetic power passing through the *X-Y* planes at 4 *Re* (red) and 15 *Re* (blue). In Figure 5b, the volume integral was performed in the rectangular volume bounded by $X = -10$ to -20 *Re*, $Y = -3$ to 3 *Re*, and $Z = 4$–15 *Re*. In Figure 5c, the surface integral was performed in the area bounded by $X = -10$ to -20 *Re* and $Y = -3$ to 3 *Re*.

magnetospheric convection, we may be able to say that the near-Earth dynamo, which is a consequence of the NENL, is embedded in the convection system.

Figure 4 shows $\nabla \cdot \mathbf{V}_\perp$ and $\nabla \cdot \mathbf{S}$ in the meridional plane at midnight. At 15 min before the onset (Figure 4, left column), $\nabla \cdot \mathbf{V}_\perp$ and $\nabla \cdot \mathbf{S}$ are systematically negative in the large part of the lobe. Negative values of $\nabla \cdot \mathbf{V}_\perp$ and $\nabla \cdot \mathbf{S}$ mean an increase in the magnetic energy or magnetic field according to equations (9) and (11). (The absolute value of $\mathbf{J} \cdot \mathbf{E}$ is very small in the lobe.) At the onset (Figure 4, right column), $\nabla \cdot \mathbf{V}_\perp$ and $\nabla \cdot \mathbf{S}$ are systematically positive in some part of the lobe, for example, at $X = -10$ *Re* and $Z = 5$ *Re*. This change exhibits a part of the loading-unloading process. The red lines indicate the trajectories of a plasma element given by $\int \mathbf{V}_\perp(t)dt$, which is probably associated with the path of the electromagnetic energy. The red dot indicates the position of the plasma element. The plasma elements are located in the lobe at 15 min before the onset, whereas they are located in the inner magnetosphere at the onset. A part of the electromagnetic energy released in the lobe seems to traverse the separatrix as the magnetic field reconnects and go into the inner magnetosphere.

Figure 5 summarizes the integrated energy. Figure 5a shows the electromagnetic power passing thorough the spherical surface at the geocentric distance of 3.5 *Re* (positive outward). The surface integral, $\int \mathbf{S} \cdot d\mathbf{A}$, where $\mathbf{A}$ is the area vector normal to the surface (looking outward), was performed over the nightside region. The electromagnetic power penetrating into the spherical surface remains at ~5.0–5.5 $\times 10^{11}$ W, whereas it increases during the expansion phase by ~10^{11} W. This is consistent with the observation (Sun, Ahn, & Akasofu, 1985). Figure 5b shows $\partial(B^2/2\mu_0)/\partial t$, $\mathbf{J} \cdot \mathbf{E}$, and $\nabla \cdot \mathbf{S}$ integrated over the rectangular volume (box) bounded by $X = -10$ to -20 *Re*, $Y = -3$ to 3 *Re*, and $Z = 4$ to 15 *Re*. The box is located in the northern lobe. At $t < 56$ min, the magnetic energy increases in the lobe (positive power), which corresponds to the convergence of the Poynting flux ($\nabla \cdot \mathbf{S} < 0$). At the onset, the magnetic energy decreases (negative power), corresponding to the divergence of the Poynting flux ($\nabla \cdot \mathbf{S} > 0$). Dynamo effect ($\mathbf{J} \cdot \mathbf{E} < 0$) remains scarce inside the lobe. Figure 5c shows the *Z* component of the integrated Poynting flux passing through the upper plane (at $Z = 15$ *Re*) and lower plane (at $Z = 4$ *Re*) of the box. The surface integral was performed over the top and bottom sides of the box, that is, the area bounded by $X = -10$ to -20 *Re* and $Y = -3$ to 3 *Re*. The negative value means the electromagnetic energy pointing toward the equatorial plane. At $t < 50$ min, the Poynting flux at $Z = 15$ *Re* (incoming flux) exceeds that at $Z = 4$ *Re* (outgoing flux). This implies that the Poynting flux is partially stagnated, and the magnetic energy is stored. At $t \sim 42$ min, the magnetic field configuration starts to be changed largely near the region where the near-Earth neutral line will form. At $t \sim 48$ min, the NENL starts to form. After a while, the outgoing flux (red line) exceeds the incoming flux (blue line), which implies the release of the magnetic energy. It is emphasized that a large amount of the electromagnetic power with magnitude of 0.7–1.1 $\times 10^{11}$ W steadily comes in through the upper plane ($Z = 15$ *Re*, blue line) throughout the growth and the expansion phases. It is speculated that two types of the Poynting flux are transported from the lobe toward the equatorial plane during the expansion phase. One is the energy previously stored, which is associated with the partial stagnation of the Poynting flux. The other one is the energy steadily supplied from the cusp/mantle dynamo. The amount of the released energy is estimated to be ~1.6 $\times 10^{11}$ W, which is comparable to that additionally supplied to the ionosphere after the onset. From these variations, there certainly exists the so-called loading-unloading process supported by tail magnetic field. The loading-unloading process generates a considerable fraction of Poynting flux additionally supplied to the ionosphere after the onset.

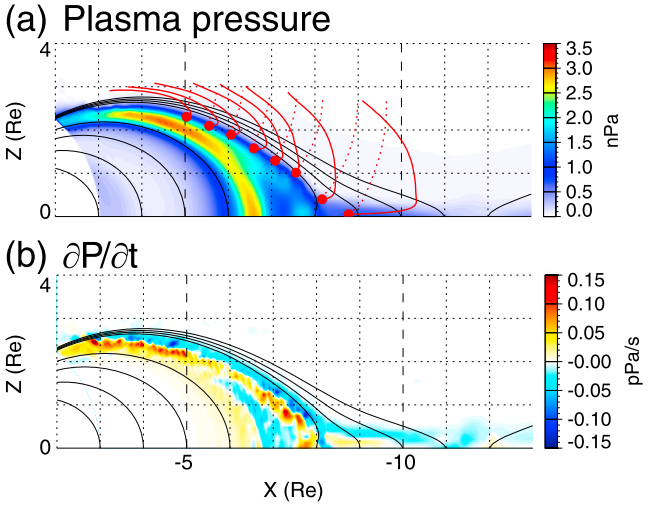

Figure 6. (a) Plasma pressure P and (b) rate of change in plasma pressure $\partial P/\partial t$ in the meridional plane at midnight at onset $t = 57.3$ min. The black line indicates a magnetic field line. The solid, red line indicates the trajectory of a plasma element, which is a line integral of the plasma velocity **V** with respect to time for 5 min. The dashed, red line is the same as the solid, red line except for the perpendicular plasma velocity $\mathbf{V}_\perp$.

3.3. Energetics in the Near-Earth Region

As shown in Figure 3, a drastic change in the pathway is found in the near-Earth region on the nightside. To see the energetics in the near-Earth region in detail, we first present Figure 6 showing the plasma pressure P and the rate of change in the plasma pressure $\partial P/\partial t$ in the meridional plane at midnight at $t = 57.3$ min. The black lines indicate the magnetic field lines. The plasma pressure increases significantly, in particular, in the inner magnetosphere. The increase in the plasma pressure is primarily attributed to the compression of plasma (not shown). We note that the plasma pressure is not necessarily constant along a field line because this is a transient phenomenon, and it takes a finite time to reach the steady condition in which the isotropic plasma pressure is constant along a field line. The decrease in the plasma pressure (e.g., at $X = -7.0$ *Re* and $Z = 1.3$ *Re*) is primarily caused by the advection of low-pressure plasma coming from the lobe. The solid, red lines indicate the trajectories of plasma elements, which are given by $\int \mathbf{V}(t)dt$. The line integral was performed backward in time from the onset $t = 57.3$ min to $t = 52.3$ min. The plasma originating in the lobe (inflow region) traverses separatrix as the magnetic field reconnects, and moves to the outflow region, as shown in Figure 1 of Eastwood et al. (2013) and Figure 5 of Zweibei and Yamada (2016). Only the earthward flow is shown in Figure 6a. For reference, the dashed, red lines indicate the trajectories given by $\int \mathbf{V}_\perp(t)dt$, where $\mathbf{V}_\perp$ is the perpendicular velocity. The dashed, red lines are tangential to the instantaneous Poynting flux **S**, suggesting the penetration of the Poynting flux into the inner magnetosphere.

Figure 7 summarizes $\mathbf{V}\cdot(\mathbf{J}\times\mathbf{B} - \nabla P)$, $\mathbf{V}\cdot\nabla P$, and $\mathbf{V}\cdot(\mathbf{J}\times\mathbf{B})$ in the meridional plane at midnight at onset ($t = 57.3$ min). Similar plots were also presented by Birn and Hesse (2005) and Tanaka et al. (2017). At midnight, the following features are noticeable.

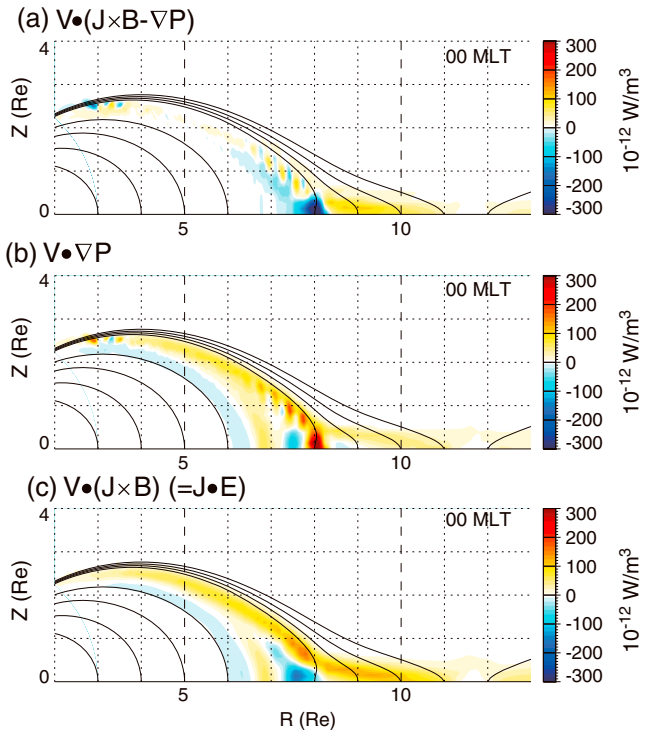

Figure 7. (a) $\mathbf{V}\cdot(\mathbf{J}\times\mathbf{B} - \nabla P)$, (b) $\mathbf{V}\cdot\nabla P$, and (c) $\mathbf{V}\cdot(\mathbf{J}\times\mathbf{B})$ in the meridional plane at midnight at onset $t = 57.3$ min. $R = (X^2 + Y^2)^{1/2}$.

1. Near the equatorial plane closed to the NENL (e.g.,, at $R = 10$ and $Z = 0$ *Re*), the electromagnetic energy splits into the thermal energy and the kinetic energy ($\mathbf{V}\cdot(\mathbf{J}\times\mathbf{B}) > 0$, $\mathbf{V}\cdot\nabla P > 0$, and $\mathbf{V}\cdot(\mathbf{J}\times\mathbf{B} - \nabla P) > 0$). This is consistent with the simulation results by Birn et al. (2010) and Birn, Hesse, and Zenitani (2011).
2. Near the equatorial plane closer to the Earth (e.g., at $R = 8$ *Re* and $Z = 0$ *Re*), the kinetic energy is converted to the thermal energy and the electromagnetic energy ($\mathbf{V}\cdot(\mathbf{J}\times\mathbf{B} - \nabla P) < 0$, $\mathbf{V}\cdot\nabla P > 0$, and $\mathbf{V}\cdot(\mathbf{J}\times\mathbf{B}) < 0$). This is probably associated with flow braking (Haerendel, 1992; Shiokawa et al., 1997).
3. In the near-Earth region at off equator (e.g., at $R = 5.0$ *Re* and $Z = 2.3$ *Re* and at $R = 7.0$ *Re* and $Z = 1.3$ *Re*), the electromagnetic energy is converted to the thermal energy ($\mathbf{V}\cdot(\mathbf{J}\times\mathbf{B}) > 0$ and $\mathbf{V}\cdot\nabla P > 0$). A similar tendency ($\mathbf{V}\cdot(\mathbf{J}\times\mathbf{B}) > 0$ and $\mathbf{V}\cdot\nabla P > 0$) is found in the inner region, for example, at $R = 5.0$ *Re* and $Z = 2.3$ *Re*. This may be associated with the Region 2-sense FACs, which is beyond the scope of this study.

Figure 8 is the same as Figure 7 except for 2318 MLT (onset meridian). At the onset meridian (2318 MLT), the following feature is noticeable.

4. The thermal energy is further converted to the electromagnetic energy ($\mathbf{V}\cdot\nabla P < 0$ and $\mathbf{V}\cdot(\mathbf{J}\times\mathbf{B}) < 0$) at off-equator (e.g., at $R = 5.2$ *Re* and $Z = 2.2$ *Re*). This is pointed out by Birn and Hesse (2005). This is near-Earth dynamo, which is in close relation with the onset FAC (Ebihara & Tanaka, 2015a, 2015b; Tanaka, 2015).

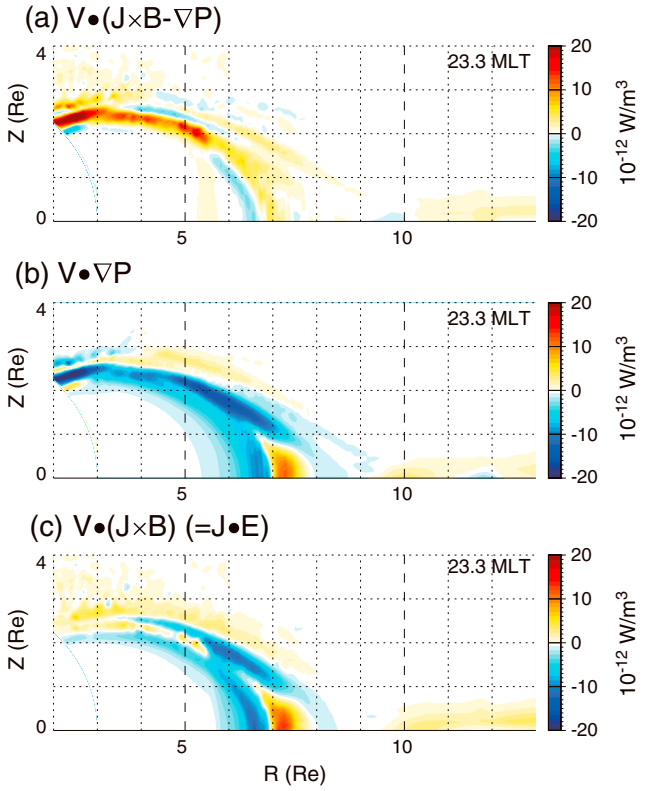

Figure 8. Same as Figure 7 except for 2318 MLT (at onset meridian).

The energy conversion is associated with mechanical work done by $\mathbf{V} \cdot \nabla P$, $\mathbf{V} \cdot (\mathbf{J} \times \mathbf{B} - \nabla P)$, and $\mathbf{V} \cdot (\mathbf{J} \times \mathbf{B})$. It is obvious that the plasma flow velocity **V** is important to evaluate the mechanical work and energy conversion.

3.4. Pathway of Energy in the Near-Earth Region

In order to understand the pathway and conversion of energy in the near-Earth region, we present Figure 9 showing a perspective view of the magnetosphere at the onset (t = 57.3 min). The thick lines indicate magnetic field lines, and the thin lines indicate integral curves of the velocity **V**. The integral curve of **V** is a curve that is tangential to instantaneous **V** and is given by $\int \mathbf{V} \cdot d\mathbf{s}/V$, where s is a line element. This is a snapshot, so that the integral curve of **V** is different from the trajectory of a plasma element. However, we think that the use of the integral curve is valuable to visualize the instantaneous direction of the velocity and to estimate approximate path of the plasma. In Figure 9 (top), the colored horizontal plane indicates the X component of the velocity in the equatorial plane. In Figure 9 (bottom), the colored plane indicates $\nabla \cdot \mathbf{S}$. The fast earthward flow is found because of the presence of reconnection. Two integral curves of **V** are drawn. They are denoted by Roman numerical figures (i) and (ii), respectively. The integral curve of **V** (i) comes from the lobe, gets close to the plasma sheet, and moves toward the Earth. As the plasma enters into the plasma sheet, the thermal energy and the kinetic energy increase ($\nabla \cdot \mathbf{H} > 0$ and $\nabla \cdot \mathbf{K} > 0$). The energy is converted from the electromagnetic energy as shown in Figure 3. As the plasma proceeds in the plasma sheet toward the Earth, the kinetic energy decreases ($\nabla \cdot \mathbf{K} < 0$) because of the mechanical work ($\mathbf{V} \cdot (\mathbf{J} \times \mathbf{B} - \nabla P) < 0$), according to equation (13). The deceleration of plasma results in compression of plasma and an increase in the plasma pressure as shown by the grey surface. Then, the kinetic energy is converted to the thermal energy and the electromagnetic energy ($\nabla \cdot \mathbf{H} > 0$ and $\nabla \cdot \mathbf{S} > 0$). The integral curve of **V** (ii) also comes from the lobe and traverses the separatrix as the magnetic field reconnects. When it approaches the high-pressure region (grey surface), it turns to the west at off-equator. The perpendicular motion of the integral curve of **V** (ii) can also be explained below. As the plasma moves toward the region where the plasma pressure is high (high-pressure region as denoted by grey surface), the thermal energy increases ($\nabla \cdot \mathbf{H} > 0$) due to the mechanical work ($\mathbf{V} \cdot \nabla P > 0$). As the plasma leaves the high-pressure region moving westward, the thermal energy decreases ($\nabla \cdot \mathbf{H} < 0$), and the electromagnetic energy increases due to the mechanical work ($\mathbf{V} \cdot (\mathbf{J} \times \mathbf{B}) < 0$ or $\mathbf{J} \cdot \mathbf{E} < 0$), that is, the dynamo. The magnetic field line extending from the onset (onset field line) is also indicated by a thick line colored with (top) $\mathbf{J} \cdot \mathbf{E}$ and (bottom) $J_{\parallel}$. This dynamo region is found to coexist with upward FACs at off-equator as shown in Figure 9 (bottom). It can be said from Figure 9 that the electromagnetic energy is also generated in the near-Earth region on the nightside in association of two types of flow shear. One is associated with the flow shear near the equatorial plane as indicated by the integral curve (i). The other is associated with the flow shear at off-equator as indicated by the integral curve (ii).

Figure 10 summarizes the plasma pressure, parallel vorticity, FACs, and $\mathbf{J} \cdot \mathbf{E}$ in the Y-Z plane at $X = -5$ Re. The plasma pressure is high at $Z < 2.4$ Re, and the increase in the plasma pressure is attributed to the compression (not shown). In Figure 10b, the parallel vorticity is present. The perpendicular flow velocity is indicated by the arrow. The plasma coming from the lobe traverses the separatrix as the magnetic field reconnects near the equatorial plane (as is shown in Figures 4 and 6). Then, the flow splits into the westward one and the eastward one. The westward flow is responsible for the positive vorticity and upward FAC as shown in Figure 10c. The upward Region 1-sense FAC appears on the westside of the high-pressure region that is centered at $Z \sim 2$ Re. A pair of the Region 1-sense FACs is found in the high-latitude part of the high-pressure region indicated in Figure 10a. The flow associated with the upward Region 1-sense FAC corresponds to the integral curve of **V** (ii) shown in Figure 9. The dynamo region ($\mathbf{J} \cdot \mathbf{E} < 0$) is embedded in the upward FAC region including the point (−5.0, 1.0, 2.3) Re at which the magnetic field line extending from the onset position passes through.

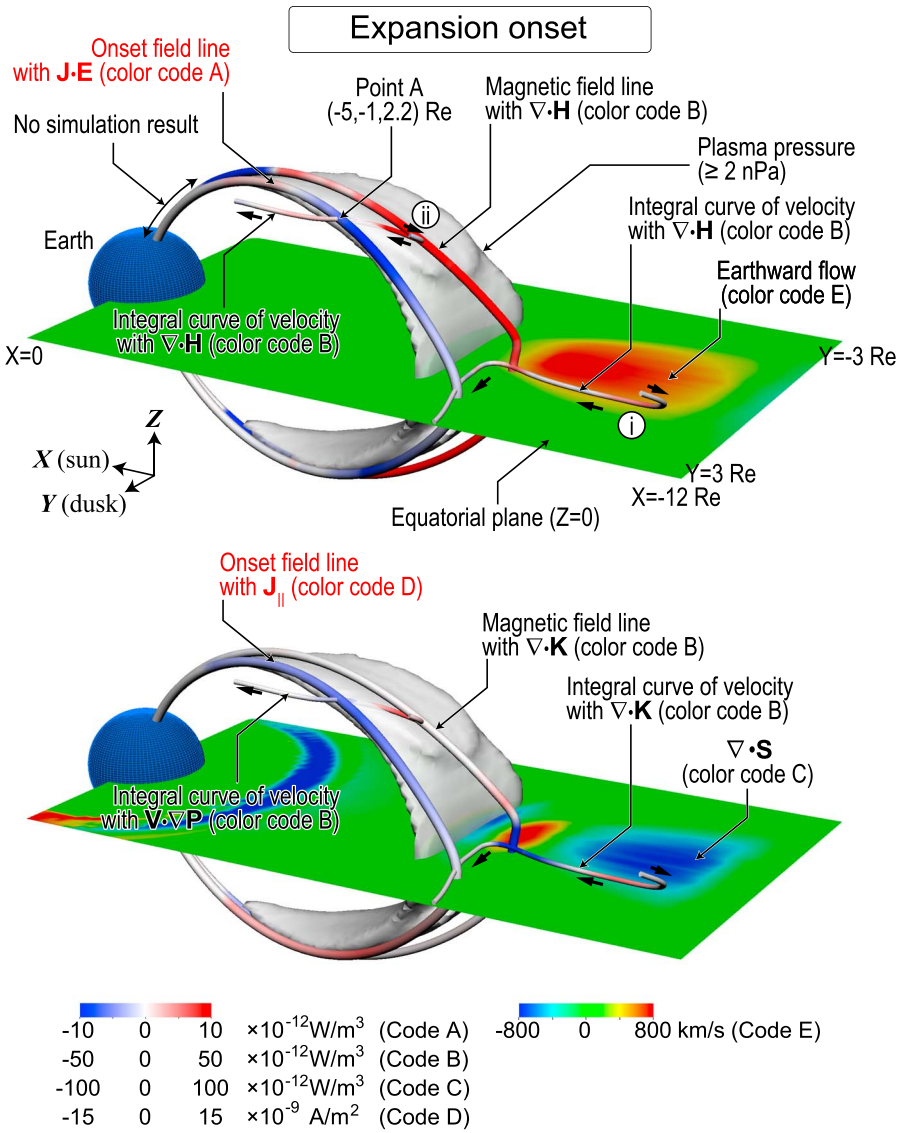

Figure 9. Perspective view of the magnetosphere at expansion onset (t = 57.3 min). The blue sphere indicates the Earth. The thick lines indicate magnetic field lines, and the thin lines indicate integral curves of the velocity of plasma. Onset field line represents the magnetic field line extending from the onset position (cross in Figure 1). The magnetic field lines and the integral curves are colored with physical quantities: (top) $\mathbf{J} \cdot \mathbf{E}$, $\nabla \cdot \mathbf{H}$ and (bottom) $J_{\parallel}$ (field-aligned current), $\mathbf{V} \cdot \nabla P$, $\nabla \cdot \mathbf{K}$. The grey surface is an isopressure surface at 2 nPa. The X component of the plasma flow and $\nabla \cdot \mathbf{S}$ are shown in the equatorial plane in the top and bottom panels, respectively.

The eastward one is responsible for the negative vorticity and downward FAC. A pair of the Region 2-sense FACs is also found in the low-latitude part of it.

Figure 11 summarizes the quantities related to energetics taking along the trajectory of plasma. The trajectory was obtained by integrating the velocity with respect to time $\int \mathbf{V}(t)dt$ backward in time. The integration was performed from the point A at (−5, 1, 2.2) Re at t = 57.3 min. The point A is indicated in Figure 9. The point A belongs to the dynamo region ($\mathbf{J} \cdot \mathbf{E} < 0$). The trajectory considers time-dependent velocity, which is morphologically similar to the integral curve of $\mathbf{V}$ (ii) shown in Figure 9. We note that due to unwanted numerical errors, these quantities do not exactly satisfy equations (11), (13), and (14). The plasma came from the high-latitude magnetosphere where the plasma pressure is low. As the plasma moves from the lobe toward the point A, $\mathbf{V} \cdot \nabla P$ increases together with $\mathbf{V} \cdot (\mathbf{J} \times \mathbf{B})$ until $t \sim 56.5$ min. The good coincidence between $\mathbf{V} \cdot \nabla P$ and $\mathbf{V} \cdot (\mathbf{J} \times \mathbf{B})$ probably indicates that the electromagnetic energy

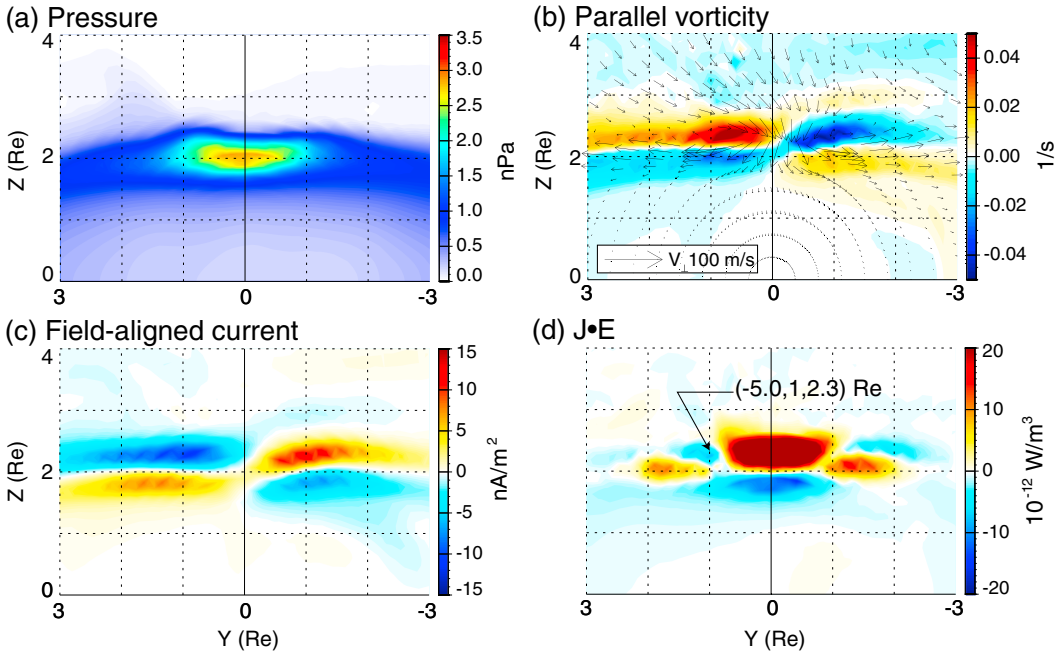

Figure 10. (a) Plasma pressure, (b) parallel vorticity $\Omega_{\parallel}$, (c) field-aligned current $J_{\parallel}$, and (d) $\mathbf{J} \cdot \mathbf{E}$ in the *Y-Z* plane at $X = -5$ *Re* at onset (t = 57.3 min). In Figure 10b, the arrow indicates the perpendicular flow velocity mapped on the *Y-Z* plane.

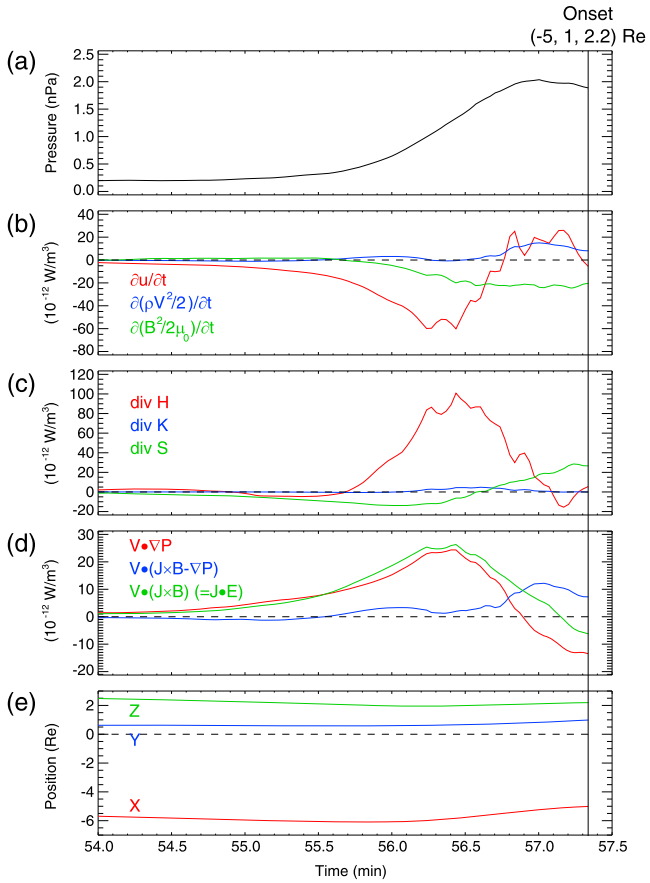

Figure 11. (a) Plasma pressure, (b) $\partial u/\partial t$, $\partial(\rho V^2/2)/\partial t$ and $\partial(B^2/2\mu_0)/\partial t$, (c) $\nabla \cdot \mathbf{H}$, $\nabla \cdot \mathbf{K}$, and $\nabla \cdot \mathbf{S}$, (d) $\mathbf{V} \cdot \nabla P$, $\mathbf{V}$ ($\mathbf{J} \times \mathbf{B} - \nabla P$), and $\mathbf{V}$ ($\mathbf{J} \times \mathbf{B}$), and (e) position. They are taken along the trajectory of a plasma element backward in time, starting at (−5, 1, 2.2) *Re* and t = 57.3 min.

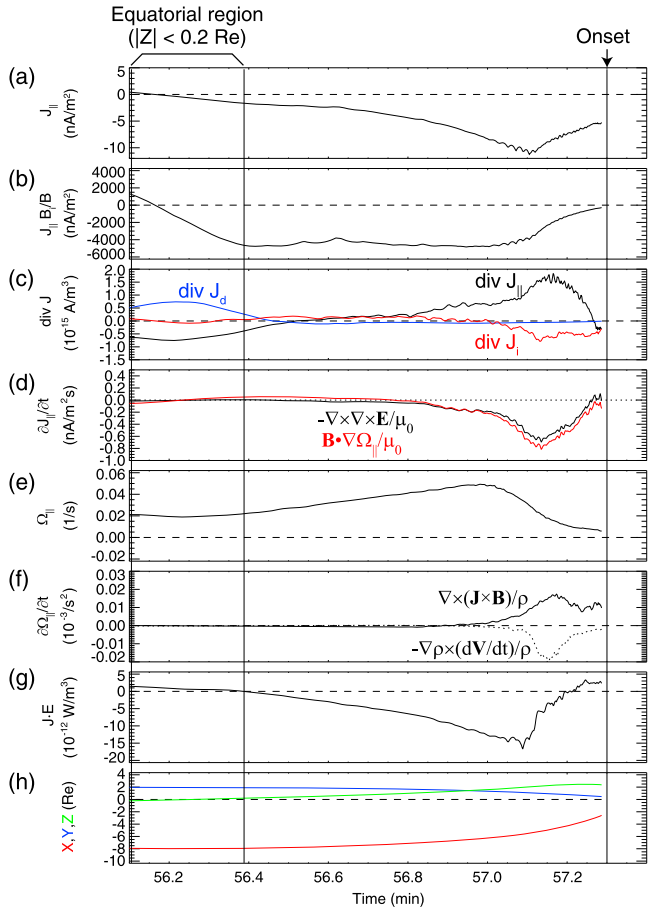

Figure 12. (a) FAC (negative upward); (b) normalized FAC; (c) divergence of the current density: divergence of FAC (black), divergence of diamagnetic current (blue), and divergence of inertial current (red); (d) rate of change in the FAC; (e) parallel vorticity; (f) rate of change in parallel vorticity due to two terms; (g) $\mathbf{J} \cdot \mathbf{E}$; and (h) position of the field line. These quantities are taken along a path of the Alfvén wave transmitted backward in time from the onset position and the onset time indicated by the vertical line on the right-hand side. The region near the far left edge bounded by the vertical line on the left-hand side indicates the equatorial plane ($|Z| < 0.2$ *Re*).

is converted to the thermal energy. Near the point *A* ($t \sim 57.3$ min), $\mathbf{V}\cdot(\mathbf{J} \times \mathbf{B} - \nabla P) > 0$, $\mathbf{V}\cdot(\mathbf{J} \times \mathbf{B}) < 0$, and $\mathbf{V} \cdot \nabla P < 0$. This probably means that the thermal energy splits into the kinetic energy and the electromagnetic energy. The dynamo ($\mathbf{J} \cdot \mathbf{E} < 0$) is evident at $t > 57.1$ min.

3.5. Generation of Field-Aligned Current

Finally, we focused on the origin of the upward FACs that manifests the expansion onset in the ionosphere shown in Figure 1. In order to find the relevant region where the upward FACs are generated, we traced a possible path of the Alfvén wave backward in time because the FACs are thought to be closely associated with Alfvén waves (Song & Lysak, 2001a, 2001b). The possible path $\mathbf{R}(t)$ was obtained by solving the equation

$$\mathbf{R}(t) = a \int_{t_0}^{t} \left[V_A(\tau, \mathbf{r}) \frac{\mathbf{B}(\tau, \mathbf{r})}{B(\tau, \mathbf{r})} \right] \mathrm{d}\tau, \tag{17}$$

where V_A is the local speed of the Alfvén wave being $B/\sqrt{\mu_0 \rho}$, t_0 is the onset time (57.3 min), and a is a constant being 1 or -1 depending on the direction of the integral. Since the starting point was situated in the Northern Hemisphere and $\mathrm{d}\tau < 0$, we chose 1 for a. Figure 12 summarizes relevant quantities taken along the possible path of the Alfvén wave backward from (−2.02, 0.36, 2.19) *Re* where the onset position is mapped from the ionosphere to the 3 *Re* surface along the dipole field line. (In order to evaluate the spatial derivatives numerically, we needed to start the calculation just above the inner boundary of the simulation. Only the values at the radial distance greater than 3.5 *Re* are shown.) The vertical line on the right-hand side of Figure 12 represents the starting point of the tracing (corresponding to the onset time of 57.3 min). Figure 12a shows the FAC. The negative FAC means the upward one in the Northern Hemisphere. The FAC is almost zero near the equatorial region ($|Z| < 0.2$ *Re*). The upward FAC increases with time (distance from the equatorial plane). The maximum of upward FAC takes place at (−5.5, 1.1, 2.0) *Re* (geocentric distance of 5.9 *Re*). Figure 12b shows the FAC multiplied by B_i/B, where B_i is the intensity of the magnetic field at the ionosphere. The normalized FAC, $J_\parallel'$, is introduced to show the net current flowing in a flux tube regardless of the area of the flux tube. The magnitude of $J_\parallel'$ increases near the equatorial plane, whereas $J_\parallel'$ is almost held constant from $t \sim 56.4$ to $t \sim 57.1$ min. $J_\parallel'$ starts to approach to zero at $t \sim 57.1$ min. However, $J_\parallel'$ does not reach zero at the onset. We defined the onset as the moment at which the upward FAC starts to increase in the ionosphere. Therefore, at the onset, the upward FAC just starts to increase at the inner boundary of the simulation, which leads to the increase in the upward FAC in the ionosphere in the simulation. Figure 12c shows divergence of three current density vectors, the FAC, the diamagnetic current ($\mathbf{J}_d$), and the inertial current ($\mathbf{J}_i$). They are given by

$$\mathbf{J}_\parallel = J_\parallel \frac{\mathbf{B}}{B} = \frac{\nabla \times \mathbf{B}}{\mu_0} \cdot \frac{\mathbf{B}}{B}, \tag{18}$$

$$\mathbf{J}_d = \frac{\mathbf{B} \times \nabla P}{B^2}, \tag{19}$$

and

$$\mathbf{J}_i = \rho \frac{\mathbf{B}}{B^2} \times \frac{\mathrm{d}\mathbf{V}_\perp}{\mathrm{d}t}, \tag{20}$$

respectively. The FACs are coupled to the diamagnetic current near the equatorial plane, whereas they are coupled to the inertial current at off-equator. Figure 12c only represents the continuity of the current, so

that more diagnosis is necessary to understand the generation of the upward FACs. Figure 12d shows the rates of change in the FACs $\partial J_{\parallel}/\partial t$ calculated by using two different equations (equations (4) and (6)). They are almost identical. This means that the approximation of equation (6) is valid and that the generation of the upward FAC can be reasonably explained in terms of vorticity. $\partial J_{\parallel}/\partial t$ is largely negative at off-equator, meaning that the strong upward FAC is generated at off-equator at this moment. We should note that the instantaneous FAC is not necessarily proportional to instantaneous $\partial J_{\parallel}/\partial t$ because the instantaneous FAC is a result of the integral of $\partial J_{\parallel}/\partial t$ with respect to time. It is also expected that the generation of the upward FAC results in redistribution of the ambient current and the Lorentz force that adjusts the force balance. The generation of FAC is associated with the field-aligned gradient of the vorticity $\Omega_{\parallel}$ as shown in Figure 12e. The vorticity slightly increases and peaks at off-equator at ~57.0 min. The negative gradient of the vorticity in the earthward part of the peak seems to generate the upward FACs that connect to the ionosphere, according to equation (6). Figure 12f shows rate of change in $\Omega_{\parallel}$. The solid and dotted lines indicate the first and the second terms of the right-hand side of equation (8). It is shown that, in general, the first term, curl of the Lorentz force, dominates the second term, so as to increase $\Omega_{\parallel}$. Figure 12g shows $\mathbf{J} \cdot \mathbf{E}$, indicating that $\mathbf{J} \cdot \mathbf{E}$ is largely negative at off-equator at $t \sim 56.4$–57.2 min. This corresponds to the near-Earth dynamo shown in Figure 10 and probably means that the onset FACs are primarily generated or powered at off-equator. Of course, we cannot exclude the possibility that the onset FACs are generated near the equatorial plane.

4. Discussion

First, we discuss the processes regarding the substorm expansion. The following is probably one of the most commonly accepted models to explain the expansion onset (e.g., Cowley, 2000; Kepko et al., 2015, and references therein):

1. Dayside reconnection gives rise to the transfer of open flux from the dayside to nightside. When nightside reconnection occurs in the tail region, newly closed field lines return sunward to complete the Dungey cycle.
2. A collapse or dipolarization of the stretched field lines occurs in association with reduction of the cross-tail current.
3. A current wedge appears to form as a result of a collapse of the cross-tail current or a superposition of some current loops including FACs generated by flow shear in the plasma sheet.
4. The Region 1-sense FAC newly developed on the nightside is more powered by the reduction of the magnetic field in the tail lobe than by a generator situated in the magnetosheath or at the magnetopause.

The global MHD simulation is capable of reproducing many observable features that are regarded as key manifestations of substorm expansion, for example, sudden decrease in the *AL* index, westward traveling surge, dipolarization, azimuthal deflection of the magnetic field at geosynchronous orbit, positive bay at midlatitude, and overshielding (Ebihara et al., 2014; Ebihara & Tanaka, 2015a, 2015b, 2018; Tanaka, 2015; Tanaka et al., 2010, 2017). Based on the simulation results, we discuss each of the processes.

For the item 2, the dipolarization is also found in the global MHD simulation. The dipolarization delays in the inner part of the plasma sheet. The dipolarization can take place after the onset depending on the distance from the NENL (Tanaka et al., 2017). This is consistent with the observation (Runov et al., 2009) and is discussed in detail by Tanaka et al. (2017).

For the item 3, the current wedge-like structure also appears in the global MHD simulation. However, the structure is different from the traditionally thought because the perpendicular current, including the diamagnetic current, is also intensified at the onset (Ebihara & Tanaka, 2015a, 2015b; Tanaka, 2015). By summing up the perpendicular and parallel currents, one may find that the current vector is not always aligned with the magnetic field line. If one draws a current line like a magnetic field line, the current line extending from the ionosphere at the onset position is diverted from the original field line by the perpendicular current. It does not reach the equatorial plane because the perpendicular current is strong in the plasma sheet. Braking of the earthward fast flow is suggested to cause flow shear and generate the Region 1-sense FACs in the plasma sheet (e.g., Birn et al., 2004, 2011; Birn & Hesse, 2014; Keiling et al., 2009). The flow shear at off-equator seems to be responsible for the generation of the onset field-aligned current. We cannot rule

out the possibility that the flow shear near the equatorial plane also contributes to the generation of the onset field-aligned current.

For the item 4, the pathway of the energy from the magnetospheric dynamo to the ionosphere was obscure. The plasma pressure in the inner magnetosphere (or in the inner part of the plasma sheet) is suggested to be a mediator for the energy conversion (Birn & Hesse, 2005; Haerendel, 2009; Tanaka et al., 2010, 2017; Hamrin et al., 2012; Ebihara & Tanaka, 2015a, 2015b). We think that the pathway of the energy and associated energy conversion are clearly illuminated by the global MHD simulation. This may be similar to the concept of squeezing of the magnetosphere (Haerendel, 2009).

The substorm is suggested to consist of two components, the directly driven (DD) component and the unloading (UL) component (e.g., Akasofu, 1979b). The DD component is fairly well correlated with the ε parameter, whereas the UL component is less correlated with it (Sun, Xu, & Akasofu, 1998). The DD component is known to be associated with the convection driven by reconnection, and the UL component is known to be associated with the current wedge system (Kamide & Kokubun, 1996). In the sense that the convection and the "current wedge system" are related to the cusp/mantle dynamo and the near-Earth dynamo, respectively, we can rephrase it as follows: The DD component is associated with the cusp/mantle dynamo, and the UL component is associated with the near-Earth dynamo. It seems in the simulation result that the near-Earth dynamo is embedded in the pathway of the energy from the cusp/mantle dynamo to the ionosphere, namely, convection system, as shown in Figure 3. In this sense, the expansion onset may be regarded as a sudden, localized intensification of the convection.

The simulation result is consistent with a statistical study performed by Miyashita et al. (2001, 2012) and Machida et al. (2009). The onset was determined by Pi2 pulsations (Miyashita et al., 2001) and satellite-borne auroral images (Machida et al., 2009; Miyashita et al., 2012). At off-equator, the Poynting flux pointing toward the equatorial plane began to appear at least 10 min prior to the onset and further increased ~4 min before the onset (Machida et al., 2009). The magnetic field also increased at off-equator. They defined the direction of the Poynting flux to be the same as the plasma convection. This means that the flow toward the equatorial plane began to intensify ~4 min prior to the onset. The statistical study was limited at $X = -9$ *Re* owing to the orbit of the Geotail satellite. Further study is required to confirm the simulation result that the flow shear also begins to intensify at closer distance, such as at $X = -5$ *Re*, at off-equator. The recently launched satellite, Arase (previously known as ERG), is suitable for investigating it because Arase has an orbital inclination of ~31° and the apogee of ~6 *Re*.

Ebihara and Tanaka (2015a) reported that in addition to the $\mathbf{J} \cdot \mathbf{E}$ term, part of the magnetic field energy might be converted to the electromagnetic energy flow near the leading edge of the high-pressure region at off-equator, in accordance with Poynting's theorem. Because thermal and kinetic energy must be considered together with the electromagnetic field energy, careful diagnosis is required to understand the radiation of the Poynting flux. From this perspective, we note that the description regarding the conversion of the magnetic field energy to the electromagnetic energy flow was probably incomplete, and it was too early to draw conclusions. We leave the energetics regarding the change in the magnetic field energy for future study.

5. Conclusions

The major conclusions obtained from this study are summarized as follows.

1. The Poynting flux originating from the cusp/mantle dynamo is responsible for the large-scale convection (Siscoe et al., 2000; Tanaka, 1995) and is partially stagnated in the lobe during the growth phase. After the formation of the NENL, the accumulated energy is released and is transported toward the equatorial plane. In addition to the accumulated one, a large amount of the Poynting flux is continuously supplied from the cusp/mantle dynamo toward the equatorial region by way of the lobe. The released energy is estimated to be comparable to the energy continuously supplied from the cusp/mantle dynamo.
2. Two types of pathways of energy are probably involved for the generation of the upward FACs that manifest the expansion onset. The first one is associated with the earthward flow near the equatorial plane. In the plasma sheet, the electromagnetic energy coming from the lobe splits into the thermal energy and the kinetic energy. The kinetic energy is converted to the electromagnetic energy and the thermal energy due to compression in the inner magnetosphere when the earthward flow decelerates (flow braking). This

is also discussed by Birn et al. (2010, 2011). The second one is associated with the flow at off-equator. A large part of the electromagnetic energy is converted to the thermal energy. When the plasma with large enthalpy moves toward dusk, the thermal energy is converted to the electromagnetic energy (probably by way of the kinetic energy). The first (second) type of the pathway is associated with the generation of the upward FACs near the equatorial plane (at off-equator). The onset-associated FACs are probably powered by the second one because of the presence of the near-Earth dynamo (where $\mathbf{J} \cdot \mathbf{E} < 0$) at off-equator. However, the contribution from the first one is probably nonnegligible.

3. The pathway of the electromagnetic energy is associated with the large-scale convection manifested by the *S*-curve. The near-Earth dynamo seems to be embedded in the pathway of the energy from the cusp/mantle dynamo to the ionosphere, namely, the magnetospheric convection system. In this sense, the expansion onset may be regarded as sudden, local intensification of the convection initiated by the formation of NENL.

Acknowledgments
The authors thank Professor Emeritus Atsuhiro Nishida and Professor Emeritus Takashi Kikuchi for their insightful and fruitful comments and discussion. The computer simulation was performed on the KDK computer system at the Research Institute for Sustainable Humanosphere (RISH), Kyoto University. This study was supported by JSPS KAKENHI grants 15H03732 and 15H05815. The simulation data are available at the web http://www2.rish.kyoto-u.ac.jp/~ebihara/mhd-substorm/.

References

Ahn, B. H., Robinson, R. M., Kamide, Y., & Akasofu, S. I. (1983). Electric conductivities, electric fields and auroral particle energy injection rate in the auroral ionosphere and their empirical relations to the horizontal magnetic disturbances. *Planetary and Space Science*, *31*(6), 641–653. https://doi.org/10.1016/0032-0633(83)90005-3

Akasofu, S. (2015). Auroral substorms as an electrical discharge phenomenon. *Progress in Earth and Planetary Science*, *2*(1). https://doi.org/10.1186/s40645-015-0050-9

Akasofu, S.-I. (1964). The development of the auroral substorm. *Planetary and Space Science*, *12*(4), 273–282. https://doi.org/10.1016/0032-0633(64)90151-5

Akasofu, S.-I. (1979a). Interplanetary energy flux associated with magnetospheric substorms. *Planetary and Space Science*, *27*(4), 425–431. https://doi.org/10.1016/0032-0633(79)90119-3

Akasofu, S.-I. (1979b). What is a magnetospheric substorm? In *Dynamics of the Magnetosphere* (pp. 447–460). Norwell, Mass: D.Reidel. https://doi.org/10.1007/978-94-009-9519-2_23

Akasofu, S.-I. (1980). The solar wind-magnetosphere energy coupling and magnetospheric disturbances. *Planetary and Space Science*, *28*(5), 495–509. https://doi.org/10.1016/0032-0633(80)90031-8

Akasofu, S.-I. (2003). A source of auroral electrons and the magnetospheric substorm current systems. *Journal of Geophysical Research*, *108*(A4), 8006. https://doi.org/10.1029/2002JA009547

Akasofu, S.-I., Kamide, Y., Kan, J. R., Lee, L. C., & Ahn, B.-H. (1981). Power transmission from the solar wind-magnetosphere dynamo to the magnetosphere and to the ionosphere: Analysis of the IMS Alaska meridian chain data. *Planetary and Space Science*, *29*(7), 721–730. https://doi.org/10.1016/0032-0633(81)90042-8

Angelopoulos, V., McFadden, J. P., Larson, D., Carlson, C. W., Mende, S. B., Frey, H., … Kepko, L. (2008). Tail reconnection triggering substorm onset. *Science*, *321*, 931–935. https://doi.org/10.1126/science.1160495

Armstrong, J. C., Akasofu, S.-I., & Rostoker, G. (1975). A comparison of satellite observations of Birkeland currents with ground observations of visible aurora and ionospheric currents. *Journal of Geophysical Research*, *80*(4), 575–586. https://doi.org/10.1029/JA080i004p00575

Arnoldy, R. L. (1974). Auroral particle precipitation and Birkeland currents. *Reviews of Geophysics*, *12*(2), 217–231. https://doi.org/10.1029/RG012i002p00217

Atkinson, G. (1967). An approximate flow equation for geomagnetic flux tubes and its application to polar substorms. *Journal of Geophysical Research*, *72*(21), 5373–5382. https://doi.org/10.1029/JZ072i021p05373

Axford, W. I., & Hines, C. O. (1961). A unifying theory of high-latitude geophysical phenomena and geomagnetic storms. *Canadian Journal of Physics*, *39*(10), 1433–1464. https://doi.org/10.1139/p61-172

Baker, D. N., Pulkkinen, T. I., McPherron, R. L., Craven, J. D., Frank, L. A., Elphinstone, R. D., … Nagai, T. (1993). CDAW 9 analysis of magnetospheric events on May 3, 1986: Event C. *Journal of Geophysical Research*, *98*(A3), 3815–3834. https://doi.org/10.1029/92JA02475

Birn, J., Borovsky, J. E., Hesse, M., & Schindler, K. (2010). Scaling of asymmetric reconnection in compressible plasmas. *Physics of Plasmas*, *17*(5), 052108. https://doi.org/10.1063/1.3429676

Birn, J., & Hesse, M. (1991). The substorm current wedge and field-aligned currents in MHD simulations of magnetotail reconnection. *Journal of Geophysical Research*, *96*(A2), 1611–1618. https://doi.org/10.1029/90JA01762

Birn, J., & Hesse, M. (2005). Energy release and conversion by reconnection in the magnetotail. *Annales de Geophysique*, *23*, 3,365–3,373. https://doi.org/10.5194/angeo-23-3365-2005

Birn, J., & Hesse, M. (2014). The substorm current wedge: Further insights from MHD simulations. *Journal of Geophysical Research: Space Physics*, *119*, 3503–3513. https://doi.org/10.1002/2014JA019863

Birn, J., Hesse, M., & Zenitani, S. (2011). Reconnection in compressible plasmas: Extended conversion region. *Physics of Plasmas*, *18*, 111202. https://doi.org/10.1063/1.3626836

Birn, J., Nakamura, R., Panov, E. V., & Hesse, M. (2011). Bursty bulk flows and dipolarization in MHD simulations of magnetotail reconnection. *Journal of Geophysical Research*, *116*, A01210. https://doi.org/10.1029/2010JA016083

Birn, J., Raeder, J., Wang, Y. L., Wolf, R. A., & Hesse, M. (2004). On the propagation of bubbles in the geomagnetic tail. *Annales de Geophysique*, *22*, 1773–1786. https://doi.org/10.5194/angeo-22-1773-2004

Boström, R. (1964). A model of the auroral electrojets. *Journal of Geophysical Research*, *69*(23), 4983–4999. https://doi.org/10.1029/JZ069i023p04983

Brice, N. M. (1967). Bulk motion of the magnetosphere. *Journal of Geophysical Research*, *72*(21), 5193–5211. https://doi.org/10.1029/JZ072i021p05193

Chen, C. X., & Wolf, R. A. (1993). Interpretation of high-speed flows in the plasma sheet. *Journal of Geophysical Research*, *98*(A12), 21,409–21,419. https://doi.org/10.1029/93JA02080

Connors, M., McPherron, R. L., Anderson, B. J., Korth, H., Russell, C. T., & Chu, X. (2014). Electric currents of a substorm current wedge on 24 February 2010. *Geophysical Research Letters*, *41*, 4449–4455. https://doi.org/10.1002/2014GL060604

Cowley, S. W. H. (2000). Magnetosphere-ionosphere interactions: A tutorial review. In S.-I. Ohtani, et al. (Eds.), *Magnetospheric Current Systems* (Vol. 118, pp. 91–106). Washington, DC: American Geophysical Union. https://doi.org/10.1029/GM118p0091

Davis, T. N., & Sugiura, M. (1966). Auroral electrojet activity index *AE* and its universal time variations. *Journal of Geophysical Research*, *71*(3), 785–801. https://doi.org/10.1029/JZ071i003p00785

Dungey, J. W. (1961). Interplanetary magnetic field and the auroral zones. *Physical Review Letters*, *6*(2), 47–48. https://doi.org/10.1103/PhysRevLett.6.47

Eastwood, J. P., Phan, T. D., Øieroset, M., Shay, M. A., Malakit, K., Swisdak, M., … Masters, A. (2013). Influence of asymmetries and guide fields on the magnetic reconnection diffusion region in collisionless space plasmas. *Plasma Physics and Controlled Fusion*, *55*(12), 124001. https://doi.org/10.1088/0741-3335/55/12/124001

Ebihara, Y., & Tanaka, T. (2015a). Substorm simulation: Insight into the mechanisms of initial brightening. *Journal of Geophysical Research: Space Physics*, *120*, 7270–7288. https://doi.org/10.1002/2015JA021516

Ebihara, Y., & Tanaka, T. (2015b). Substorm simulation: Formation of westward traveling surge. *Journal of Geophysical Research: Space Physics*, *120*, 10,466–10,484. https://doi.org/10.1002/2015JA021697

Ebihara, Y., & Tanaka, T. (2018). Why does substorm-associated auroral surge travel westward? *Plasma Physics and Controlled Fusion*, *60*(1), 014024. https://doi.org/10.1088/1361-6587/aa89fd

Ebihara, Y., Tanaka, T., & Kikuchi, T. (2014). Counter equatorial electrojet and overshielding after substorm onset: Global MHD simulation study. *Journal of Geophysical Research: Space Physics*, *119*, 7281–7296. https://doi.org/10.1002/2014JA020065

Elphinstone, R. D., Hearn, D., Murphree, J. S., & Cogger, L. L. (1991). Mapping using the Tsyganenko long magnetospheric model and its relationship to Viking auroral images. *Journal of Geophysical Research*, *96*(A2), 1467–1480. https://doi.org/10.1029/90JA01625

Fujii, R., Amm, O., Yoshikawa, A., Ieda, A., & Vanhamäki, H. (2011). Reformulation and energy flow of the Cowling channel. *Journal of Geophysical Research*, *116*, A02305. https://doi.org/10.1029/2010JA015989

Gjerloev, J. W., & Hoffman, R. A. (2014). The large-scale current system during auroral substorms. *Journal of Geophysical Research: Space Physics*, *119*, 4591–4606. https://doi.org/10.1002/2013JA019176

Haerendel, G. (1992). Disruption, ballooning or auroral avalanche—On the cause of substorms. In *Proceedings of the First International Conference on Substorms* (pp. 417–420). Kiruna: ESA Publications Division.

Haerendel, G. (2009). Poleward arcs of the auroral oval during substorms and the inner edge of the plasma sheet. *Journal of Geophysical Research*, *114*, A06214. https://doi.org/10.1029/2009JA014138

Hamrin, M., Marghitu, O., Norqvist, P., Buchert, S., André, M., Klecker, B., … Dandouras, I. (2012). The role of the inner tail to midtail plasma sheet in channeling solar wind power to the ionosphere. *Journal of Geophysical Research*, *117*, A06310. https://doi.org/10.1029/2012JA017707

Hones, E. W. Jr., Asbridge, J. R., Bame, S. J., & Singer, S. (1973). Substorm variations of the magnetotail plasma sheet from $X_{SM} \approx -6\ R_E$ to $X_{SM} \approx -60\ R_E$. *Journal of Geophysical Research*, *78*(1), 109–132. https://doi.org/10.1029/JA078i001p00109

Hones, E. W. Jr. (1984). Plasma sheet behavior during substorms. In E. W. Hones Jr. (Ed), *Magnetic Reconnection in Space and Laboratory Plasmas* (pp. 178–184). Washington, DC: AGU.

Iijima, T., & Potemra, T. A. (1976). The amplitude distribution of field-aligned currents at northern high latitudes observed by Triad. *Journal of Geophysical Research*, *81*(13), 2165–2174. https://doi.org/10.1029/JA081i013p02165

Kadokura, A., A. S. Yukimatu, M. Ejiri, T. Oguti, M. Pinnock, & M. R. Hairston (2002). Detailed analysis of a substorm event on 6 and 7 June 1989: 1. Growth phase evolution of nightside auroral activities and ionospheric convection toward expansion phase onset. *Journal of Geophysical Research*, *107*(A12), 1479. https://doi.org/10.1029/2001JA009127

Kamide, Y., & Akasofu, S.-I. (1975). The auroral electrojet and global auroral features. *Journal of Geophysical Research*, *80*(25), 3585–3602. https://doi.org/10.1029/JA080i025p03585

Kamide, Y., & Akasofu, S.-I. (1976). The location of the field-aligned currents with respect to discrete auroral arcs. *Journal of Geophysical Research*, *81*(22), 3999–4003. https://doi.org/10.1029/JA081i022p03999

Kamide, Y., Craven, J. D., Frank, L. A., Ahn, B.-H., & Akasofu, S.-I. (1986). Modeling substorm current systems using conductivity distributions inferred from DE auroral images. *Journal of Geophysical Research*, *91*(A10), 11,235–11,256. https://doi.org/10.1029/JA091iA10p11235

Kamide, Y., & Kokubun, S. (1996). Two-component auroral electrojet: Importance for substorm studies. *Journal of Geophysical Research*, *101*(A6), 13,027–13,046. https://doi.org/10.1029/96JA00142

Kamide, Y., Richmond, A. D., & Matsushita, S. (1981). Estimation of ionospheric electric fields, ionospheric currents, and field-aligned currents from ground magnetic records. *Journal of Geophysical Research*, *86*(A2), 801–813. https://doi.org/10.1029/JA086iA02p00801

Kamide, Y., Sun, W., & Akasofu, S.-I. (1996). The average ionospheric electrodynamics for the different substorm phases. *Journal of Geophysical Research*, *101*(A1), 99–109. https://doi.org/10.1029/95JA02990

Kan, J. R. (1993). A global magnetosphere-ionosphere coupling model of substorms. *Journal of Geophysical Research*, *98*(A10), 17,263–17,275. https://doi.org/10.1029/93JA01168

Kan, J. R., & Kamide, Y. (1985). Electrodynamics of the westward traveling surge. *Journal of Geophysical Research*, *90*(A8), 7615–7619. https://doi.org/10.1029/JA090iA08p07615

Kan, J. R., Lee, L. C., & Akasofu, S.-I. (1980). The energy coupling function and the power generated by the solar wind-magnetosphere dynamo. *Planetary and Space Science*, *28*(8), 823–825. https://doi.org/10.1016/0032-0633(80)90080-X

Kan, J. R., & Sun, W. (1996). Substorm expansion phase caused by an intense localized convection imposed on the ionosphere. *Journal of Geophysical Research*, *101*(A12), 27,271–27,281. https://doi.org/10.1029/96JA02426

Kan, J. R., Williams, R. L., & Akasofu, S.-I. (1984). A mechanism for the westward traveling surge during substorms. *Journal of Geophysical Research*, *89*(A4), 2211–2216. https://doi.org/10.1029/JA089iA04p02211

Kaufmann, R. L. (2012). Dependence of plasma sheet energy fluxes and currents on solar wind-magnetosphere coupling. *Journal of Geophysical Research*, *117*, A10230. https://doi.org/10.1029/2012JA017995

Keiling, A., Angelopoulos, V., Runov, A., Weygand, J., Apatenkov, S. V., Mende, S., … Auster, H. U. (2009). Substorm current wedge driven by plasma flow vortices: THEMIS observations. *Journal of Geophysical Research*, *114*, A00C22. https://doi.org/10.1029/2009JA014114.

Kepko, L., McPherron, R. L., Amm, O., Apatenkov, S., Baumjohann, W., Birn, J., … Sergeev, V. (2015). Substorm current wedge revisited. *Space Science Reviews*, *190*(1-4), 1–46. https://doi.org/10.1007/s11214-014-0124-9

Lui, A. T. Y. (1991). A synthesis of magnetospheric substorm models. *Journal of Geophysical Research*, *96*(A2), 1849–1856. https://doi.org/10.1029/90JA02430

Lui, A. T. Y. (1996). Current disruption in the Earth's magnetosphere: Observations and models. *Journal of Geophysical Research*, *101*(A6), 13,067–13,088. https://doi.org/10.1029/96JA00079

Lui, A. T. Y. (2011). Reduction of the cross-tail current during near-Earth dipolarization with multisatellite observations. *Journal of Geophysical Research*, *116*, A12239. https://doi.org/10.1029/2011JA017107

Lui, A. T. Y., & Burrows, J. R. (1978). On the location of auroral arcs near substorm onsets. *Journal of Geophysical Research*, *83*(A7), 3342–3348. https://doi.org/10.1029/JA083iA07p03342

Lui, A. T. Y., Chang, C.-L., Mankofsky, A., Wong, H.-K., & Winske, D. (1991). A cross-field current instability for substorm expansions. *Journal of Geophysical Research*, *96*, 11,389–11,401. https://doi.org/10.1029/91JA00892

Lui, A. T. Y., & Y. Kamide (2003). A fresh perspective of the substorm current system and its dynamo. *Geophysical Research Letters*, *30*(18), 1958. https://doi.org/10.1029/2003GL017835

Lyatsky, W., Cogger, L. L., Jackel, B., Hamza, A. M., Hughes, W. J., Murr, D., & Rasmussen, O. (2001). Substorm development as observed by Interball UV imager and 2-D magnetic array. *Journal of Atmospheric and Solar-Terrestrial Physics*, *63*(15), 1609–1621. https://doi.org/10.1016/S1364-6826(01)00045-1

Machida, S., Miyashita, Y., Ieda, A., Nosé, M., Nagata, D., Liou, K., … Mukai, T. (2009). Statistical visualization of the Earth's magnetotail based on Geotail data and the implied substorm model. *Annales de Geophysique*, *27*, 1035–1046. https://doi.org/10.5194/angeo-27-1035-2009

McPherron, R. L., & Chu, X. (2016). Relation of the auroral substorm to the substorm current wedge. *Geoscience Letters*, *3*(1), 12. https://doi.org/10.1186/s40562-016-0044-5

McPherron, R. L., Russell, C. T., & Aubry, M. P. (1973). Satellite studies of magnetospheric substorms on August 15, 1968: 9. Phenomenological model for substorms. *Journal of Geophysical Research*, *78*(16), 3131–3149. https://doi.org/10.1029/JA078i016p03131

Miyashita, Y., Machida, S., Mukai, T., Saito, Y., & Sutcliffe, P. R. (2001). Mass and energy transport in the near and middistant magnetotail around substorm onsets: Geotail observations. *Journal of Geophysical Research*, *106*(A4), 6259–6274. https://doi.org/10.1029/2000JA000233

Miyashita, Y., Machida, S., Nosé, M., Liou, K., Saito, Y., & Paterson, W. R. (2012). A statistical study of energy release and transport midway between the magnetic reconnection and initial dipolarization regions in the near-Earth magnetotail associated with substorm expansion onsets. *Journal of Geophysical Research*, *117*, A11214. https://doi.org/10.1029/2012JA017925

Murphy, K. R., Mann, I. R., Rae, I. J., Waters, C. L., Frey, H. U., Kale, A., … Korth, H. (2013). The detailed spatial structure of field-aligned currents comprising the substorm current wedge. *Journal of Geophysical Research: Space Physics*, *118*, 7714–7727. https://doi.org/10.1002/2013JA018979

Nagai, T., Fujimoto, M., Saito, Y., Machida, S., Terasawa, T., Nakamura, R., … Kokubun, S. (1998). Structure and dynamics of magnetic reconnection for substorm onsets with Geotail observations. *Journal of Geophysical Research*, *103*(A3), 4419–4440. https://doi.org/10.1029/97JA02190

Nielsen, E., & Greenwald, R. A. (1979). Electron flow and visual aurora at the Harang discontinuity. *Journal of Geophysical Research*, *84*(A8), 4189–4200. https://doi.org/10.1029/JA084iA08p04189

Nishida, A., & Nagayama, N. (1973). Synoptic survey for the neutral line in the magnetotail during the substorm expansion phase. *Journal of Geophysical Research*, *78*(19), 3782–3798. https://doi.org/10.1029/JA078i019p03782

Østgaard, N., Germany, G., Stadsnes, J., & Vondrak, R. R. (2002). Energy analysis of substorms based on remote sensing techniques, solar wind measurements, and geomagnetic indices. *Journal of Geophysical Research*, *107*(A9), 1233. https://doi.org/10.1029/2001JA002002

Palmroth, M., Janhunen, P., Pulkkinen, T. I., Aksnes, A., Lu, G., Østgaard, N., … Germany, G. A. (2005). Assessment of ionospheric joule heating by GUMICS-4 MHD simulation, AMIE, and satellite-based statistics: Towards a synthesis. *Annales de Geophysique*, *23*, 2051–2068. https://doi.org/10.5194/angeo-23-2051-2005

Pu, Z. Y., Korth, A., & Kremser, G. (1992). Plasma and magnetic field parameters at substorm onsets derived from GEOS 2 observations. *Journal of Geophysical Research*, *97*(A12), 19,341–19,349. https://doi.org/10.1029/92JA01732

Richmond, A. D., Kamide, Y., Akasofu, S. I., Alcaydé, D., Blanc, M., de la Beaujardière, O., … Zaitzev, A. N. (1990). Global measures of ionospheric electrodynamic activity inferred from combined incoherent scatter radar and ground magnetometer observations. *Journal of Geophysical Research*, *95*(A2), 1061–1071. https://doi.org/10.1029/JA095iA02p01061

Rostoker, G., Armstrong, J. C., & Zmuda, A. J. (1975). Field-aligned current flow associated with intrusion of the substorm-intensified westward electrojet into the evening sector. *Journal of Geophysical Research*, *80*(25), 3571–3579. https://doi.org/10.1029/JA080i025p03571

Roux, A., Perraut, S., Robert, P., Morane, A., Pedersen, A., Korth, A., … Pellinen, R. (1991). Plasma sheet instability related to the westward traveling surge. *Journal of Geophysical Research*, *96*(A10), 17,697–17,714. https://doi.org/10.1029/91JA01106

Runov, A., Angelopoulos, V., Sitnov, M. I., Sergeev, V. A., Bonnell, J., McFadden, J. P., … Auster, U. (2009). THEMIS observations of an earthward-propagating dipolarization front. *Geophysical Research Letters*, *36*, L14106. https://doi.org/10.1029/2009GL038980

Russell, C. T., & McPherron, R. L. (1973). The magnetotail and substorms. *Space Science Reviews*, *15*(2-3), 205–266. https://doi.org/10.1007/BF00169321

Sakanoi, T., Fukunishi, H., & Mukai, T. (1995). Relationship between field-aligned currents and inverted-V parallel potential drops observed at midaltitudes. *Journal of Geophysical Research*, *100*(A10), 19,343–19,360. https://doi.org/10.1029/95JA01285

Samson, J. C., Lyons, L. R., Newell, P. T., Creutzberg, F., & Xu, B. (1992). Proton aurora and substorm intensifications. *Geophysical Research Letters*, *19*(21), 2167–2170. https://doi.org/10.1029/92GL02184

Samson, J. C., Wallis, D. D., Hughes, T. J., Creutzberg, F., Ruohoniemi, J. M., & Greenwald, R. A. (1992). Substorm intensifications and field line resonances in the nightside magnetosphere. *Journal of Geophysical Research*, *97*(A6), 8495–8518. https://doi.org/10.1029/91JA03156

Sergeev, V., Kubyshkina, M., Alexeev, I., Fazakerley, A., Owen, C., Baumjohann, W., … Lucek, E. (2008). Study of near-Earth reconnection events with Cluster and Double Star. *Journal of Geophysical Research*, *113*, A07S36. https://doi.org/10.1029/2007JA012902

Shay, M. A., Drake, J. F., Eastwood, J. P., & Phan, T. D. (2011). Super-Alfvénic propagation of substorm reconnection signatures and Poynting flux. *Physical Review Letters*, *107*, 65,001. https://doi.org/10.1103/PhysRevLett.107.065001

Schindler, K. (1974). A theory of the substorm mechanism. *Journal of Geophysical Research*, *79*(19), 2803–2810. https://doi.org/10.1029/JA079i019p02803

Shiokawa, K., Baumjohann, W., & Haerendel, G. (1997). Braking of high-speed flows in the near-Earth tail. *Geophysical Research Letters*, *24*(10), 1179–1182. https://doi.org/10.1029/97GL01062

Siscoe, G. L., Crooker, N. U., Erickson, G. M., Sonnerup, B. U. Ö., Siebert, K. D., Weimer, D. R., … Maynard, N. C. (2000). Global geometry of magnetospheric currents. In S.-I. Ohtani, et al. (Eds.), *Magnetospheric Current Systems*, *Geophysical Monograph Series* (Vol. 118, pp. 41–52). Washington, DC: American Geophysical Union. https://doi.org/10.1029/GM118p0041

Song, Y., & Lysak, R. L. (2001a). Towards a new paradigm: From a quasi-steady description to a dynamical description of the magnetosphere. *Space Science Reviews*, *95*(1/2), 273–292. https://doi.org/10.1023/A:1005288420253

Song, Y., & Lysak, R. L. (2001b). The physics in the auroral dynamo regions and auroral particle acceleration. *Physics and Chemistry of the Earth*, *26*, 33.

Strangeway, R. J., Elphic, R. C., Peria, W. J., & Carlson, C. W. (2000). FAST observations of electromagnetic stresses applied to the polar ionosphere. In S.-I. Ohtani, et al. (Eds.), *Magnetospheric Current Systems*, *Geophysical Monograph Series* (Vol. 118, pp. 21–29). Washington, DC: American Geophysical Union. https://doi.org/10.1029/GM118p0021

Sun, W., Ahn, B.-H., & Akasofu, S.-I. (1985). The global Joule heat production rate and the *AE* index. *Planetary and Space Science*, *33*(3), 279–281. https://doi.org/10.1016/0032-0633(85)90059-5

Sun, W., Xu, S.-Y., & Akasofu, S.-I. (1998). Mathematical separation of directly-driven and unloading components in the ionospheric equivalent currents during substorms. *Journal of Geophysical Research*, *103*(A6), 11,695–11,700. https://doi.org/10.1029/97JA03458

Takahashi, K., Zanetti, L. J., Lopez, R. E., McEntire, R. W., Potemra, T. A., & Yumoto, K. (1987). Disruption of the magnetotail current sheet observed by AMPTE/CCE. *Geophysical Research Letters*, *14*(10), 1019–1022. https://doi.org/10.1029/GL014i010p01019

Tanaka, T. (1995). Generation mechanisms for magnetosphere-ionosphere current systems deduced from a three-dimensional MHD simulation of the solar wind-magnetosphere-ionosphere coupling processes. *Journal of Geophysical Research*, *100*(A7), 12,057–12,074. https://doi.org/10.1029/95JA00419

Tanaka, T. (2000). Field-aligned current systems in the numerically simulated magnetosphere. In S. Ohtani, et al. (Eds.), *Magnetospheric Current Systems*, *Geophysical Monograph Series* (Vol. 118, pp. 53–59). Washington, DC: American Geophysical Union. https://doi.org/10.1029/GM118p0053

Tanaka, T. (2007). Magnetosphere–ionosphere convection as a compound system. *Space Science Reviews*, *133*, 1–72. https://doi.org/10.1007/s11214-007-9168-4

Tanaka, T. (2015). Substorm auroral dynamics reproduced by advanced global magnetosphere−ionosphere (M-I) coupling simulation. In *Auroral Dynamics and Space Weather* (pp. 177–190). Hoboken, NJ: John Wiley, Inc. https://doi.org/10.1002/9781118978719.ch13

Tanaka, T., Den, M., Fujita, S., Ebihara, Y., Kikuchi, T., Hashimoto, K., & Kataoka, R. (2016). Generation of field-aligned current (FAC) and convection through the formation of pressure regimes: Correction for the concept of Dungey's convection. *Journal of Geophysical Research, Space Physics*, *121*, 8695–8711. https://doi.org/10.1002/2016JA022822

Tanaka, T., Ebihara, Y., Watanabe, M., Den, M., Fujita, S., Kikuchi, T., … Kataoka, R. (2017). Global simulation study for the time sequence of events leading to the substorm onset. *Journal of Geophysical Research: Space Physics*, *122*, 6210–6239. https://doi.org/10.1002/2017JA024102

Tanaka, T., Nakamizo, A., Yoshikawa, A., Fujita, S., Shinagawa, H., Shimazu, H., … Hashimoto, K. K. (2010). Substorm convection and current system deduced from the global simulation. *Journal of Geophysical Research*, *115*, A05220. https://doi.org/10.1029/2009JA014676

Tanskanen, E. I., Palmroth, M., Pulkkinen, T. I., Koskinen, H. E. J., Janhunen, P., Østgaard, N., … Liou, K. (2005). Energetics of a substorm on 15 August, 2001: Comparing empirical methods and a global MHD simulation. *Advances in Space Research*, *36*, 1825–1829. https://doi.org/10.1016/j.asr.2004.05.013

Treumann, R. A., Jaroschek, C. H., Nakamura, R., Runov, A., & Scholer, M. (2006). The role of the Hall effect in collisionless magnetic reconnection. *Advances in Space Research*, *38*, 101–111. https://doi.org/10.1016/j.asr.2004.11.045

Untiedt, J., & Baumjohann, W. (1993). Studies of polar current systems using the IMS Scandinavian magnetometer array. *Space Science Reviews*, *63*, 245–390. https://doi.org/10.1007/BF00750770

Weygand, J. M., McPherron, R. L., Frey, H., Amm, O., Kauristie, K., Viljanen, A. T., & Koistinen, A. (2008). Relation of substorm onset to Harang discontinuity. *Journal of Geophysical Research*, *113*, A04213. https://doi.org/10.1029/2007JA012537

Wing, S., Ohtani, S., Newell, P. T., Higuchi, T., Ueno, G., & Weygand, J. M. (2010). Dayside field-aligned current source regions. *Journal of Geophysical Research*, *115*, A12215. https://doi.org/10.1029/2010JA015837

Wolf, R. A., Wan, Y., Xing, X., Zhang, J.-C., & Sazykin, S. (2009). Entropy and plasma sheet transport. *Journal of Geophysical Research*, *114*, A00D05. https://doi.org/10.1029/2009JA014044

Xing, X., Liang, J., Spanswick, E., Lyons, L. R., & Angelopoulos, V. (2013). Auroral wave structures and ballooning instabilities in the plasma sheet. *Journal of Geophysical Research: Space Physics*, *118*, 6319–6326. https://doi.org/10.1002/2013JA019068

Xing, X., & Wolf, R. A. (2007). Criterion for interchange instability in a plasma connected to a conducting ionosphere. *Journal of Geophysical Research*, *112*, A12209. https://doi.org/10.1029/2007JA012535

Yang, J., Toffoletto, F. R., Wolf, R. A., Sazykin, S., Ontiveros, P. A., & Weygand, J. M. (2012). Large-scale current systems and ground magnetic disturbance during deep substorm injections. *Journal of Geophysical Research*, *117*, A04223. https://doi.org/10.1029/2011JA017415

Yao, Z. H., Pu, Z. Y., Fu, S. Y., Angelopoulos, V., Kubyshkina, M., Xing, X., … Li, J. X. (2012). Mechanism of substorm current wedge formation: THEMIS observations. *Geophysical Research Letters*, *39*, L13102. https://doi.org/10.1029/2012GL052055

Yue, C., Wang, C.-P., Nishimura, Y., Murphy, K. R., Xing, X., Lyons, L. R., … Nagai, T. (2015). Empirical modeling of 3-D force-balanced plasma and magnetic field structures during substorm growth phase. *Journal of Geophysical Research: Space Physics*, *120*, 6496–6513. https://doi.org/10.1002/2015JA021226

Zhou, X.-Y., Sun, W., Ridley, A. J., & Mende, S. B. (2011). Joule heating associated with auroral electrojets during magnetospheric substorms. *Journal of Geophysical Research*, *116*, A00I28. https://doi.org/10.1029/2010JA015804

Zou, S., Lyons, L. R., Wang, C.-P., Boudouridis, A., Ruohoniemi, J. M., Anderson, P. C., … Devlin, J. C. (2009). On the coupling between the Harang reversal evolution and substorm dynamics: A synthesis of SuperDARN, DMSP, and IMAGE observations. *Journal of Geophysical Research*, *114*, A01205. https://doi.org/10.1029/2008JA013449

Zweibei, E. G., & Yamada, M. (2016). Perspectives on magnetic reconnection. *Proceedings of the Royal Society A.*, *472*(2196), 20160479. https://doi.org/10.1098/rspa.2016.0479